



Cite this: DOI: 10.1039/c8cy02603c

Influence of Au/Pd alloy on an amine functionalised ZnCr LDH–MCM-41 nanocomposite: A visible light sensitive photocatalyst towards one-pot imine synthesis†

Dipti Prava Sahoo,^a Sulagna Patnaik,^a Dharitri Rath,^b Priyabrat Mohapatra,^c Ashutosh Mohanty^d and Kulamani Parida *^a

Achieving photocatalytic organic transformation reactions by using a visible light induced semiconductor-based photocatalyst is promising as a green and sustainable approach. In the present study, Au/Pd bimetallic alloy loaded amine (APTES) functionalised LDH (Layered double hydroxide)–MCM-41 composite was prepared through an *in situ* co-precipitation followed by a co-reduction method. The structural phases, textural properties, optical behaviour, morphological aspects, chemical states and functional groups of the photocatalysts were thoroughly analysed by powder X-ray diffraction (PXRD), high-resolution transmission electron microscopy (HRTEM), ultraviolet-visible diffuse reflectance (UV-vis DRS), fourier-transform infrared (FTIR) and X-ray photoelectron (XPS) spectroscopies. Moreover, the formation of an alloying structure between Au and Pd was confirmed from PXRD, HRTEM and UV-vis absorption spectra. We investigated one-pot synthesis of imines through photoalkylation of benzyl alcohol with nitrobenzene over Au/Pd bimetal alloy loaded on amine functionalised LDH–MCM-41 composite and it demonstrated imine yield of around 3.1 times (68%) more than the parent LDH (22%). The alloy nanoparticless efficiently harvest light and possess higher photocatalytic activity with respect to single Pd and Au nanoparticles. Due to the alloying structure develops charge heterogeneity on the surface of alloyed nanoparticles and enhances the interaction between metal surface with substrate molecule which promotes the coupling between photo generated benzaldehyde with aniline to form imine. Characterisation such as photoluminescence (PL), time-resolved photoluminescence (TRPL), electrical impedance spectroscopy (EIS) and photocurrent density measurements further proved the superior photoactivity towards imine synthesis. These photocatalytic tandem reactions, therefore, have great potential as an effective pathway for the one-pot organic synthesis and transformation of organics in an environmentally friendly way.

Received 26th December 2018,
Accepted 25th March 2019

DOI: 10.1039/c8cy02603c

rsc.li/catalysis

Introduction

Imines are a superior group of organic compounds with carbon–nitrogen bonds which are very essential intermediates of various biological, pesticides, polymer and medicine products

because they can undergo versatile organic conversions such as condensations, additions, reductions, and multi component reactions.¹ To serve these purposes, fabrication of a basic unit imine is essential. The approach to imine synthesis has been adopted through photochemical reactions and various traditional methods. Although the design of complicated organic transformations for imine formation and photochemical reactions is admirable, they are associated with low selectivity of targeted products which makes the process difficult.² Traditionally, with the support of a Lewis acid catalyst, the aldehydes/ketones undergo dehydrating condensation reactions with amines to form imines. Furthermore, with a simpler approach, dehydrogenation of secondary amines to form imines is also possible using strong oxidising agents like MnO₂ and *o*-iodoxybenzoic acid. However, adaptation of such a synthesis route provides a low stability and expensive pathway, difficulty in controlling the reaction conditions and low

^a Centre for Nano science and Nano Technology, Siksha 'O' Anusandhan Deemed to be University, Bhubaneswar-751030, Odisha, India.

E-mail: kulamaniparida@soaniversity.ac.in

^b Department of Chemistry, Rajdhani College, Bhubaneswar-751003, Odisha, India

^c Department of Chemistry, C.V.Raman College of Engineering, Bidyanagar, Mahura, Janla, Bhubaneswar-752 054, Odisha, India

^d Solid State and Structural Chemistry Unit, Indian institute of Science, Bengaluru-560012, India

† Electronic supplementary information (ESI) available. See DOI: 10.1039/c8cy02603c

selectivity of target products with many undesired by-products generated from those oxidising agents. Various research groups also have reported the quick condensation of aldehydes and amines in the presence of a Lewis acid as catalyst at room temperature, but this rapid oxidation process does not lead to a visualized successful reaction.^{3–6} To circumvent these difficulties, research has been accredited from photochemical and traditional methods to photocatalytic reactions that can be executed under easily available conditions to achieve higher product selectivity.⁷ Further, integration of a photocatalytic reaction into a tandem reaction facilitates multi-step reactions in one reactor and is considered as an active approach to enhance chemical reactions. This approach bypasses time consumption, the formation of unwanted intermediates, lengthy separation purification processes, energy utilization and loss of production.⁸ Many organic transformation reactions have been reported which are carried out in one pot tandem reactions. But, many of these engage homogeneous catalysts, resulting in contaminated products and restrict recyclability.⁹ So, our current research is focused on developing a heterogeneous photocatalytic system, involving one-pot synthesis. In this one-pot synthesis route of imines, the alkylation of benzyl alcohol (alkylating reagent) with nitrobenzene in cooperation with a heterogeneous photocatalyst is one of the most promising approaches due to easy accessibility, reasonable price, low energy consumption, environmental friendliness, reusability, and durability.⁷ In this context of one-pot imine synthesis, many visible light induced photocatalysts were studied for organic conversions that usually involved the following three consecutive steps: (i) photooxidation of benzyl alcohol to benzaldehyde, (ii) photoreduction of nitrobenzene to aniline, (iii) and finally condensation of benzaldehyde with aniline to form imine.

Moreover, noble metal (Au, Pd, Ag, Pt and Cu) supported catalysts have been efficiently used in various photocatalytic reactions such as water splitting organic conversions, organic pollutant degradation, *etc.*^{10,11} Among them, bimetallic alloy catalyst (Au/Pd) photocatalytic organic transformation reactions are important as they provide a greater activity result compared to single metal (Au/Pd) bimetallic alloy nanoparticles, which have synergistic electron interactions between them that can enhance the photocatalytic performance. Further, upon visible light irradiation by the effect of localized surface plasmon resonance (LSPR), the energetic electrons (hot electrons) are transferred from Au to Pd due to the electronegativity difference between the two atoms. As a consequence, electron availability in the Pd site proffers a good affinity for activating the reactant molecules. The charge heterogeneity on the surfaces of Au/Pd alloy nanoparticles plays a vital role in the photocatalytic reaction.¹² Various literature reports on Au/Pd alloy supported semiconductor materials like TiO₂,¹³ BiPO₄,¹⁴ g-C₃N₄,¹⁵ MOF(UiO-66(Zr_{100-x}Ti_x)),¹⁶ *etc.* describe photocatalytic reactions. Additionally, the nature of the support material is also very important in organic conversion reactions. Surface acidity and basic sites stimulate the adsorption of substrate molecules to

generate intermediate complexes which facilitate the reaction.

LDH (Layered double hydroxide) plays an important role in heterogeneous catalysis such as: (1) cation-tunability of the brucite-like layers with anionic exchangeability and (ii) tunable basicity of the surface both as Brønsted- and Lewis-type basic sites.¹⁷ Considering the surface basic properties of LDH, it has progressively received much attention in various organic transformation reactions like condensations (Knoevenagel and Aldol), transesterification and isomerisation.^{18–20} (iii) Uniform distribution of bivalent and trivalent metal cations in the brucite layer as well as preferred orientation of intercalated anions, offers the formation of highly dispersed and stable metal supported catalysts.¹⁷ Moreover LDH is a very good visible light based semiconductor photocatalyst with various important characteristics such as efficient light harvesting power, tunable band gap energy, effective electron–hole separation and improved surface reaction kinetics.²¹ Until the present, many scientists have studied Au/Pd alloy decorated LDH nanocomposites for photocatalytic and catalytic applications. Wang *et al.* reported an Au–Pd/MgAl LDH for enhancing a photocatalytic reaction towards selective oxidation of benzyl alcohol.²² Sobhana *et al.* studied Au/Pd nanoparticles decorated with LDH for photodegrading orange II from water.²³ In another study, Gao *et al.* investigated the aerobic oxidation of 5-hydroxymethylfurfural in water over a highly energetic Au/Pd loaded lanthanum-doped Ca–Mg–Al LDH catalyst in a base free medium.²⁴

Direct loading of noble metal on LDH surface leads to the formation of agglomerated metal nanoparticles. Therefore, to improve the loading of Au/Pd NPs, the surface of LDH was functionalized by amine groups. Previously, our group has studied the primary alcohol oxidation and Suzuki coupling reaction by taking a Pd(II)-immobilised diamine functionalized LDH and Pd nanoparticles anchored on amine functionalized ZnAl-LDH catalyst, respectively.^{25,26} Although LDH possesses good potential support for functionalising with amine groups, usually its surface areas is very low and cannot provide sufficient exposed surface –OH groups for the grafting of amine groups. Therefore, modification of LDH with MCM-41 gives a large surface with silanol groups and mesoporous channels which can enhance the anchoring sites for amine group attachment and also promotes the mass transport of reagents to and from the surface. Metal ions substituted in the MCM-41 framework behave as redox active sites which can be utilised for various catalytic condensation reactions.²⁷ The support material after functionalization promotes the uniform dispersion of metal ions onto the surfaces of the catalyst without aggregation. The surface functionalities not only serve as interaction sites for stabilising the metallic nanoclusters but also play a crucial role in photocatalytic organic conversions.²⁵

Based on the above considerations, in this study we tried to synthesise Au/Pd alloy nanoparticles anchored on amine (APTES) functionalised LDH/MCM-41 nanocomposite for a photocatalytic one-pot imine synthesis through the coupled

system of benzyl alcohol and nitrobenzene. The main advantages of using MCM-41 in the present study are its large mesopores which provide mass transfer and a very large surface area that allows more active sites for reactions. The Brønsted and Lewis basic sites in amine functionalized LDH/MCM-41 help to facilitate the deprotonation of surface adsorbed benzyl alcohol and precede the photocatalytic transformation reaction. Using the functionalised APTES group as a robust π -acidic monodentate nitrogen ligand for attaching covalently with $-OH$ groups of LDH and MCM-41 stabilizes the Au/Pd alloy catalyst used in photocatalytic organic conversions. The heterogenic charge distribution of Au/Pd alloyed surface may improve interactions between reactant molecules which results in a lowering of the activation energy of the reaction and increases photocatalytic conversion.

Experimental section

Materials

Zn(NO₃)₂·6H₂O (98%), Cr(NO₃)₃·6H₂O (99%), NaOH (97%), Na₂CO₃ (99.5%), cetyl trimethyl ammonium bromide (CTAB), tetraethylorthosilicate (TEOS), NH₄OH, HAuCl₄, PdCl₂, KCl, NaBH₄, benzyl alcohol, benzaldehyde, nitrobenzene, aniline, *N*-benzylideneaniline (imine) and acetonitrile were purchased from Sigma Aldrich, Acros Organics, Merck and HIMEDIA. All of the reagents were of analytically pure grade and double distilled water was used.

Synthesis of MCM-41

Briefly, CTAB (2.4 g) was dissolved in 120 mL of water at room temperature. After obtaining a clear solution, 8 mL of NH₃ solution was added to it. Then, the silica source (TEOS, 10 mL) was allowed to mix with the above solution under continuous stirring. Immediately after hydrolysis, TEOS resulted a milky slurry of white precipitate. The resultant precipitate was stirred for another 3 h and then was allowed to dry at 80 °C overnight. To remove the surfactant, the collected white powder was calcined at 550 °C for 5 h with a ramping rate of 5 °C min⁻¹.²⁸

Synthesis of ZnCr LDH-MCM-41 (LM)

The ZnCr LDH-MCM-41nanocomposite was fabricated by an *in situ* coprecipitation process. Briefly, a desired amount of MCM-41 was placed in 20 mL of water and dispersed for 30 min by ultrasonication. A 200 mL solution containing Zn(NO₃)₂·6H₂O and Cr(NO₃)₃·6H₂O with a 2 : 1 molar ratio was slowly added to the above dispersed solution. An alkali solution containing 1 M Na₂CO₃ and 1 M NaOH was added dropwise to the above suspension maintaining pH of the solution at 8–9. In order to remove the extra dissolved ions, the obtained precipitate was filtered and washed several times using distilled water. Then the product was dried at 80 °C in an air oven. The ZnCr LDH-MCM-41 nanocomposites were prepared by varying the weight ratios between LDH to MCM-41 including 0.2 : 1 (L_{0.2}M), 0.33 : 1 (L_{0.33}M) 0.5 : 1 (L_{0.5}M) and 1 : 1 (LM). For a comparison study, pure LDH was also prepared.

Synthesis of amine@ ZnCr LDH-MCM-41 (ALM)

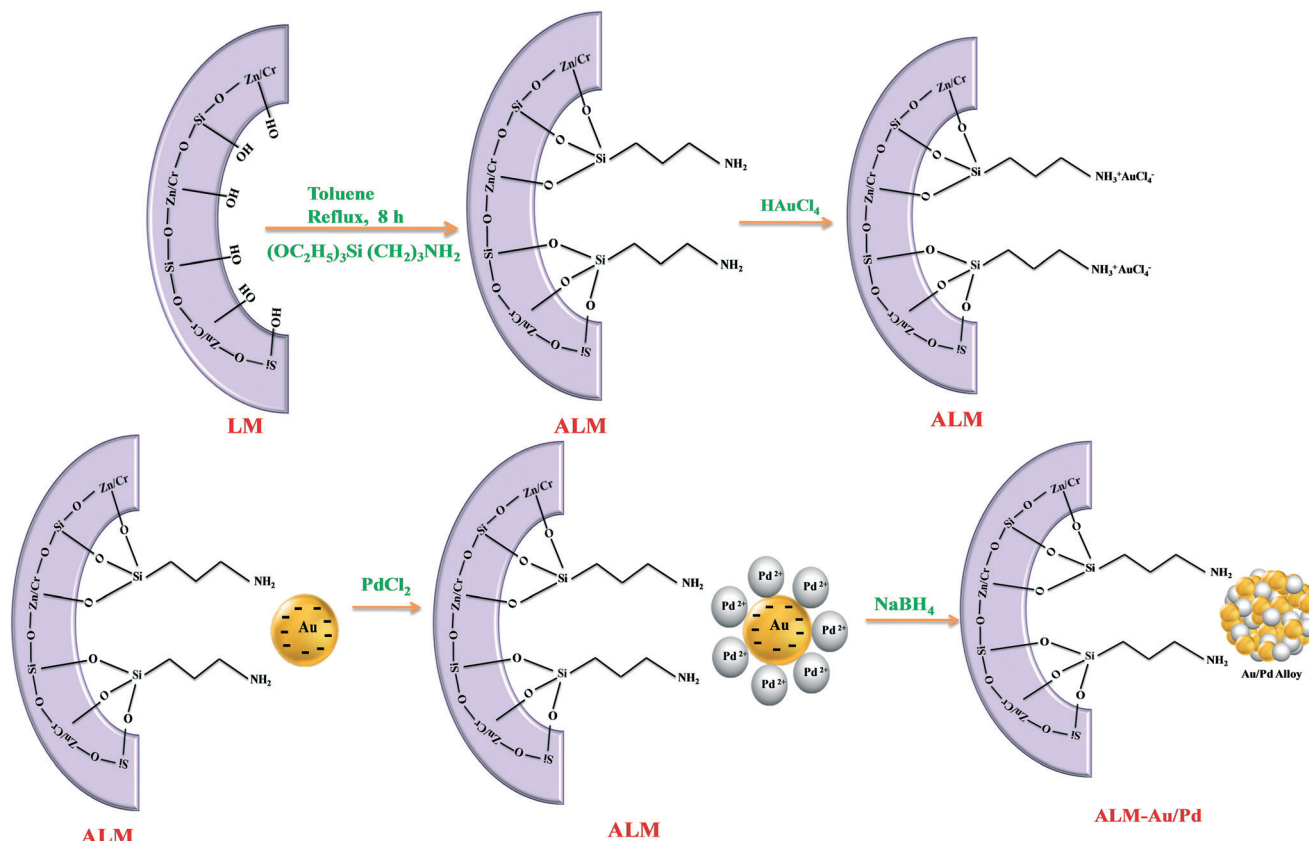
To 1 g of ZnCr LDH-MCM-41 nanocomposite (L_{0.2}M, L_{0.33}M, L_{0.5}M and LM) in 30 mL of toluene in a round-bottomed flask, 0.6 mL of APTES (amine source) was added dropwise into this suspension and refluxed for 8 h. Then, the resulting suspension was collected by centrifugation with an ethanol-water solution and dried at 35 °C for 12 h.²⁹

Synthesis of Au/Pd-amine@ ZnCr LDH-MCM-41 (ALM-Au/Pd)

After investigating the photocatalytic activity of all of the amine functionalised material (AL_{0.2}M, AL_{0.33}M, AL_{0.5}M and ALM), ALM was selected to load with noble metal nanoparticles. The ALM-Au/Pd catalyst was prepared by a reduction impregnation method, with a 1 : 1 weight ratio of Au/Pd. Then, 1 gm of ALM composite was sonicated for 30 min in 20 mL of deionised water. To load 1 wt% of both Au and Pd nanoparticles, an estimated amount of HAuCl₄, PdCl₂ and KCl (2 equiv. with respect to PdCl₂) aqueous solution was added to the above suspension and stirred for 12 h. The solid was centrifuged, washed with deionised water and collected for further use. Then, this product was redispersed in 50 mL of a NaBH₄ solution with continued stirring for another 2 h. Consequently, a dark gray coloured mass was obtained, which then was filtered and dried under vacuum. For a comparison study, monometal (Au 1 wt%, Pd 1 wt%) loaded ALM nanocomposites and Au/Pd loaded without amine functionalised LM nanocomposites were prepared by following the above procedure and denoted as ALM-Au, ALM-Pd and LM-Au/Pd respectively.³⁰

Formation mechanism of AuPd alloy on ALM composites

This synthesis procedure is illustrated in Scheme 1. As the pore walls of MCM-41 are covered with residual surface silanol groups and the brucite layers of LDH contain hydroxyl groups, the LM composite can be functionalised with organic moieties (APTES). During functionalisation a covalent bond [represented by an M–O–Si bond (M = Zn, Cr and Si)] was formed through condensation of an APTES molecule and hydroxyl group of the LM composite.³¹ After functionalisation, the organic amine groups present on the ALM surface facilitate the metal ions to uniformly anchor and form noble metal-loaded nanohybrids. Bimetallic colloids can readily synthesized by a surfactant-free co-reduction method utilizing the reducing agent NaBH₄. Usually, the metal species having the higher redox potential gets reduced first and then the second component gets reduced.³² As the reduction potential of Pd²⁺ (PdCl₄²⁻/Pd⁰ = 0.591 vs. SHE) is higher than Au³⁺ (HAuCl₄/Au⁰ = 1.008 vs. SHE), reduction of HAuCl₄ occurs first and subsequently PdCl₂ is reduced by NaBH₄. The AuCl₄⁻ with a negative charge can easily attach to the $-NH_2$ groups through a coordinate bond. Then, Pd²⁺ ions are supported on the Au lattice to form an ALM-Au/Pd nanocomposite. Owing to the chemical bonding between the Au³⁺/Pd²⁺ and $-NH_2$ groups, most of the Au³⁺ and Pd²⁺ are attached to the $-NH_2$ groups. After the addition of NaBH₄, then Au³⁺ and Pd²⁺ were reduced to metallic Au and Pd simultaneously. Owing to the whole



Scheme 1 Formation mechanism of ALM-Au/Pd.

charge, moving from Pd to Au leads to the formation of an alloy between the Au and Pd metals. Upon alloying, Pd loses s, p electrons and accepts d-electrons, whereas Au accepts s, p electrons and loses d-electrons resulting in a coulombic attraction between them.³³ Basically, formation of an alloyed bimetallic nanoparticle (Au/Pd) is dependent on the following points: (1) metal ions having approximately same redox potentials, metals with comparatively high enthalpies of mixing and nearer atomic sizes, (2) strength of bonding between the two atoms must be strong, otherwise segregation occurs, (3) surface energy is an important factor for the mixing of two hetero atoms, (4) charge transfer between low to high electronegative atoms facilitates the formation of an alloy.³⁴

Materials characterization

Using a Rigaku Miniflex powder diffractometer equipped with a Cu $K\alpha$ radiation source ($\lambda = 1.54 \text{ \AA}$), powder X-ray diffraction (PXRD) of the materials was carried out. The instrument was set at 15 mA with 30 kV and ran between the ranges of 5 to 70° at a scan rate of 2° min^{-1} . The Brunauer-Emmett-Teller (BET) surface area was analysed by the multipoint N_2 adsorption-desorption technique using a NOVA3000 (Quantachrome GmbH, Germany) instrument at a liquid N_2 temperature of 77 K. Prior to analysis, the sample was degassed for 2 h at 80 °C under vacuum to remove physically adsorbed water. Applying the Barrett-Joyner-Halenda (BJH) technique, pore size distribution and pore volumes were calculated.

The stretching and bending frequency modes of the materials were measured with the help of Fourier-transform infrared spectroscopy (JASCO FT/IR-4600) within the wavenumber range of 4000–400 cm^{-1} . A KBr matrix was used as the reference for measuring all of the samples. X-ray photoelectron spectroscopy (XPS) was carried out with a VG Microtech Multilab ESCA 3000 spectrometer. Mg $K\alpha$ X-rays were used as a non-monochromatized source. The C 1s spectra of the carbon atoms were taken as a reference for binding energy corrections. A ZEISS SUPRA55 microscope was used to obtain scanning electron microscopy (SEM) images. To determine the surface micrographs of samples, a high-resolution transmission electronic microscope (HRTEM, JEM-2100F) was used at a 200 kV accelerating voltage. To prepare the specimens, the powder samples were dispersed in ethanol (3 min) and after that this suspension was added dropwise to a carbon-coated copper grid. Optical absorbance was measured within the wavelengths of 200–800 nm on an ultraviolet-visible diffuse reflectance spectrophotometer (JASCO-V-750). A boric acid pellet was used as a reference sample. The photoluminescence (PL) behaviour of the samples was characterised using a JASCO-FP-8300 fluorescence spectrophotometer in which a xenon lamp was used as a light source. The PL spectra were obtained at room temperature at an excitation wavelength of 350 nm. Time-resolved photoluminescence (TRPL) spectra were measured using an Edinburgh Instruments FLS920 fluorescence spectrometer with a

multi-channel scaling (MCS) module equipped with a F290H pulsed xenon microsecond flash lamp.

All photoelectrochemical measurements were made using a potentiostat-galvanostatic (IVIUMnSTAT) electrochemical workstation, equipped with a 300 wt xenon lamp as the visible light source. The whole system consists of three electrode arrangements where the Pt Ag/AgCl electrodes and prepared fluorine-doped tin oxide (FTO) were taken as the counter, reference and working electrodes, respectively. FTO was made using an electrophoresis deposition method (20 mg of both sample and iodine powder were dispersed in 40 mL of acetone, then two FTOs were positioned within the solution opposite and facing parallel to each other). 0.1 M Na₂SO₄ solution was used as the electrolyte solution. The Nyquist plot was recorded at 3×10^5 Hz to 10^1 Hz at 0 bias under dark conditions and under visible light illumination. Linear sweep voltammetry (LSV) plots were recorded by applying a potential from 0–1.4 V at a scan rate of 20 mV s⁻¹ under light irradiation and dark conditions. The Mott–Schottky (MS) plot was done at a frequency of 500 Hz and chronoamperometry (CA) was performed at a potential of 0.8 V for 5 min.

Photocatalytic reaction

The photocatalytic activities of the as-synthesized catalysts were examined by the selective one pot synthesis of imines through photocatalytic oxidation and reduction of benzyl alcohol and nitrobenzene, respectively. The complete synthesis procedure was implemented as follows: 0.05 g of material was added to 10 mL of acetonitrile containing benzyl alcohol (3 mmol) and nitrobenzene (1 mmol), and then mixture was illuminated under visible light in an irradiation chamber (BS-02, Germany) for 3 h. Then, the mixed suspension was stirred vigorously for 30 min in dark conditions before visible light irradiation to maintain chemisorption equilibrium between the substrates and photocatalyst. A 250 W medium pressure Hg lamp was equipped as the light source and a 1 M NaNO₂ solution used as cut-off filter ($\lambda \geq 420$ nm). The reaction temperature was adjusted to 35–40 °C by circulating cold water during the experiment. At the end of the reaction, the solution mixture was centrifuged to remove the sample particles. Then, this resultant reaction solution was qualitatively analysed by gas chromatography (GC, Thermo scientific Trace 1110) and quantitatively determined with a gas chromatograph-mass spectrometer (GC-MS, Thermo Scientific Trace 1300). The conversion rate of benzyl alcohol and nitrobenzene, yield of benzaldehyde, imine, aniline and the reaction selectivity were calculated using the following eqn (1)–(4).

$$\text{Benzyl alcohol or nitrobenzene conversion (\%)} = \left(\frac{C_0 - C_1}{C_0} \right) \times 100 \quad (1)$$

$$\text{Benzaldehyde or aniline yield (\%)} = \left(\frac{C_2}{C_0} \right) \times 100 \quad (2)$$

$$\text{Imine yield} = \left(\frac{\text{moles of imine compound}}{\text{moles of initial nitrobenzene}} \right) \times 100 \quad (3)$$

$$\text{Benzaldehyde, aniline or imine selectivity (\%)} = \left[\frac{C_2}{(C_0 - C_1)} \right] \times 100 \quad (4)$$

Here, C_0 is the initial concentration of reactants (benzyl alcohol and nitrobenzene), C_1 is the amount of benzyl alcohol and nitrobenzene after photocatalytic reaction, whereas C_2 is the concentration of generated benzaldehyde and aniline at the end of reaction. Theoretically, the yield of imine is decided by the amount of nitrobenzene used initially.³⁵

Results and discussion

PXRD analysis was performed to investigate the structural properties, phase purity and crystalline characters of the resulting composite materials in comparison to the parent LDH. Fig. 1a shows the PXRD patterns of LDH, MCM-41 and low angle PXRD pattern of MCM-41 (inserted). LDH clearly exhibited the characteristic diffraction patterns at 2θ values of 11.5°, 23.43°, 34.3°, 38.8°, 47.3°, 59.6° and 61.1° corresponding to the (003), (006), (012), (015), (018), (110) and (113) basal planes, indicating the formation of crystalline ZnCr LDH with a hydrotalcite-like structure matching JCPDS (JCPDS: 41-1428).³⁶ Bragg reflections show that LDH has R_3m rhombohedral symmetry with several contents of a Zn/Cr octahedral lattice. The basal spacing d_{003} plane indexed as carbonate intercalated LDH close to its value of 0.77 nm. From contributions of the diffraction planes (110) and (003), the lattice parameters $a = 2d_{110}$ and $c = 3d_{003}$ were determined. The PXRD patterns of MCM-41 (low angle inserted) showed three distinct peaks: a (100) diffraction plane indicating the typical mesoporous structure and other two characteristic reflections (110) and (200) having less intense peaks representing the hexagonal periodic long range order lattice of MCM-41.³⁷ A broad peak at 2θ of 23.0° in the high angle diffraction of MCM-41 explained the amorphous framework of MCM-41. After the composite formation between LDH and MCM-41, the intensity of all the peaks of LDH drastically decreased (Fig. 1b). In particular, the d_{003} Bragg's plane of LDH became less intense and broad suggesting a negative influence of MCM-41 on the crystallinity of LDH which results in stacking defects and imperfections in the ab plane along with the c -axis of LDH. MCM-41 had a more pronounced effect controlling the LDH crystal growth direction, which reveals poor crystallinity.³⁸ After amine functionalisation, the same PXRD patterns were maintained, indicating a well ordered structural arrangement. Due to the low loading of Au and Pd nanoparticles with good dispersion on the support, the characteristic diffraction patterns of Au and Pd are not prominent. Moreover, the overlapping of diffraction patterns of

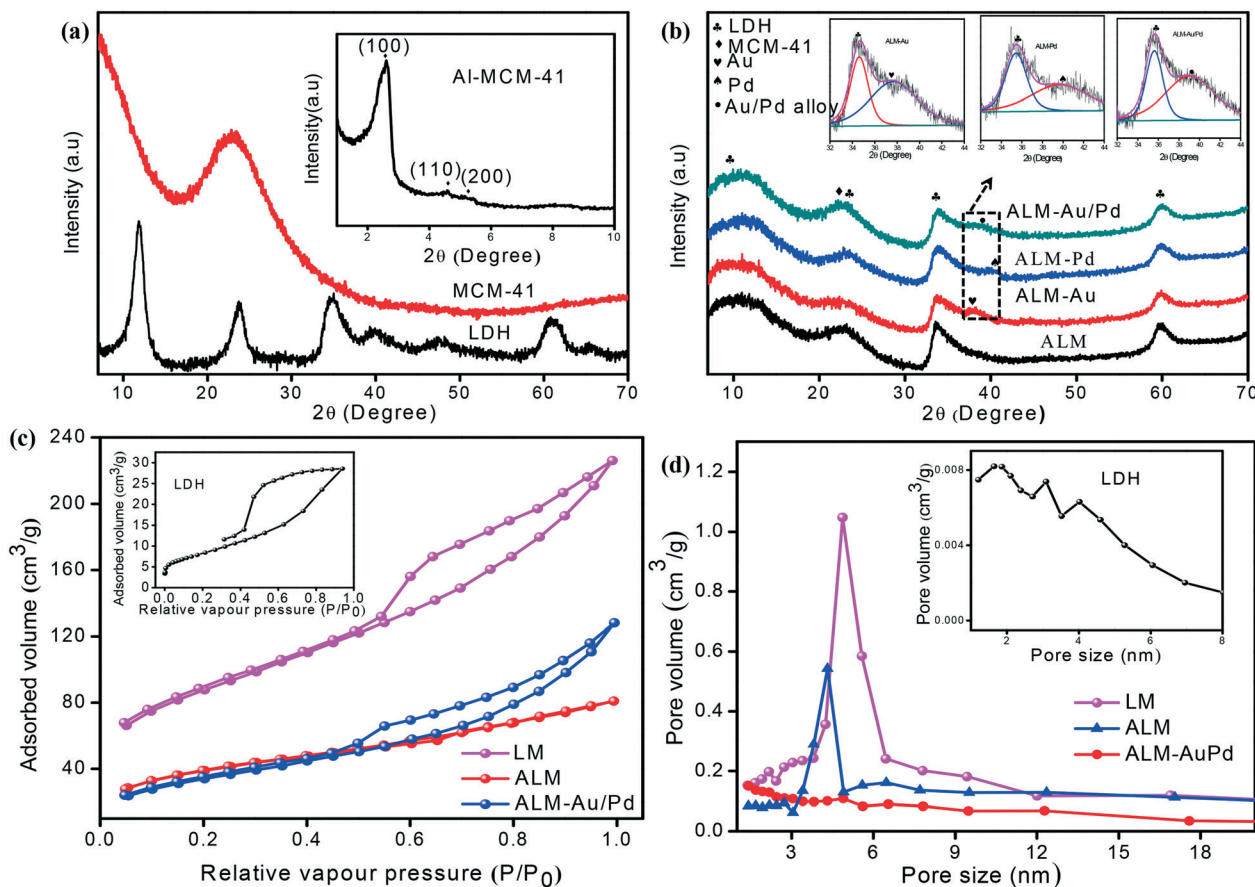


Fig. 1 PXRD patterns of LDH and MCM-41 (a), ALM, ALM-Au, ALM-Pd and ALM-Au/Pd (b), N_2 adsorption-desorption isotherms (c) and pore size distributions (d) of LDH (inserted), LM, ALM and ALM-Au/Pd.

neat LDH and noble metal nanoparticles in the cases of ALM-Au and ALM-Pd results in the appearance of a broad intense peak at around the 2θ value of $38-40^\circ$. Upon deconvolution, the presence of two diffraction patterns confirmed the loading of Au and Pd on the ALM support. The inserted PXRD image in Fig. 1b shows two peaks at 38° and at 40° representing the (111) basal planes of Au and Pd nanoparticles, respectively. However, upon loading bimetallic Au/Pd nanoparticles, a weak broad diffraction peak between a 2θ of 38° to 40° was observed. Although these two peaks in the case of monometallic ALM are very broad, the peak position in the case of bimetallic alloyed nanoparticles clearly indicated an intermediate scattering angle (the (111) basal planes of ALM-Au, ALM-Pd and ALM-Au/Pd are deconvoluted and inserted in Fig. 1b). In addition, a slight shift in the diffraction peaks of the bimetallic nanoparticles was observed from ALM-Au to ALM-Pd. This confirmed the formation of Au-Pd alloy nanoparticles in the ALM-Au/Pd nanocomposite rather than a simple mixture of bi-metal nanoparticles. The Pd nanoparticles entered into the crystal lattice of Au nanoparticles resulting in the formation of alloyed nanoparticles due to a slight mismatch in their structures. The Au lattice has a tendency to capture the Pd lattice, revealing the close interaction between them which also helped to produce the

Au/Pd alloy.^{39,40} Mean crystallite sizes of noble metal nanoparticles were calculated using the Scherrer formula by considering the (111) peak of ALM-Au, ALM-Pd and ALM-Au/Pd nanocomposites with the help of full width at half maximum. The crystallite sizes of Au, Pd and Au/Pd alloy nanoparticles were found to be 3.0, 1.97 and 2.1 nm, respectively. The decrease in the crystallite size of the bimetallic alloyed nanoparticles in comparison to monometallic Au may be due to a difference in the velocity of growth of the individual monometallic nanoparticles. As the ionization potential of Pd nanoparticles (8.33 eV) is lower than the ionization potential of Au nanoparticles (9.22 eV), incorporation of Pd inhibits the growth of bimetallic alloyed nanoparticles.⁴¹ The PXRD results demonstrated the successful creation of Au/Pd alloy nanoparticles on the surface of an ALM nanocomposite, which produced a better photocatalyst for organic transformation reactions.

The N_2 adsorption-desorption technique is a common method to determine the mesoporous behaviour and textural properties of catalysts. This study provided information about the approximate pore diameters, specific surface areas, and pore volumes *etc.* Fig. 1c and d show the N_2 isotherm and pore size distribution plots of LDH (inserted), LM, ALM and ALM-Au/Pd. Table 1 summarises the textural specifications of the

Table 1 Textural properties of MCM-41, LDH, LM, ALM and ALM-Au/Pd

Samples	Specific surface area (m ² g ⁻¹)	Pore size (nm)	Pore volume (cm ³ g ⁻¹)
MCM-41	878	3.4	0.65
LDH	28.7	1.64	0.04
LM	305.7	4.59	0.35
ALM	136.7	4.31	0.20
ALM-AuPd	124.4	4.7	0.12

samples obtained from N₂ adsorption/desorption isotherms analysis. By using BET and BJH methods specific surface areas and pore sizes of materials were calculated. According to the IUPAC classification, the shape of all the graphs suggests a type IV isotherm which confirms the mesoporous nature of the materials. During N₂ adsorption-desorption, a narrow hysteresis loop (type H3) at a relative vapour pressure range from 0.4–1 was obtained.⁴² This confirmed presence of aggregated plate-like mesoporous material, giving rise to irregular pores with non-uniform sizes. Maximum adsorption was observed at a relative pressure of $P/P^0 = 1$. According to our previous literature, the obtained specific surface area and pore size of MCM-41 were found to be 878 m² g⁻¹ and 3.4 nm, respectively.³⁷ As shown in Table 1, neat LDH showed a surface area of 28.7 m² g⁻¹. The pore size distributions were relatively narrow and found to be 1.64 nm. After modifying LDH with MCM-41, the surface area (305.7 m² g⁻¹) was drastically decreased more than MCM-41 but significantly increased from that of the LDH material; this information suggests that the active sites of LDH were uniformly distributed over the MCM-41 support and will behave as a good base catalyst. The homologous structure of LM was due to the uniform nucleation and growth in an end-facing way.³⁸ After the functionalisation of APTES on the surface of LM, the surface area also remarkably decreased. This reason was associated with the bonding of organic moiety APTES groups with Si-OH and Zn/Cr-OH in the framework of ALM sample, which revealed the surface coverage of the parent material.⁴³ Additionally, the introduction of Au/Pd alloy to the ALM surface resulted to some extent of pore blocking and decreased the surface area and pore volume also but there was an increase in number of active sites, which is beneficial for photocatalytic activity. The pore size distribution of all samples was calculated to be 3–7 nm, which suggests that all the parent and nanocomposites were in the mesoporous range.

The surface micrographs of ALM-Au/Pd were investigated by SEM analysis. Fig. S1† depicts the image of LDH, ALM and ALM-Au/Pd nanocomposites. Pure LDH appeared as a large assemblage of flaky-sheet-array laying on top of one another owing to hydroxide compounds prepared by a co-precipitation method.^{36,44} As shown in Fig. S2b,† after functionalisation of ALM by an organic moiety followed by heterostructure formation between MCM-41 and LDH, it displayed irregular shapes with loosely agglomerated particles. However, the immobilisation of noble metal particles on the surface of ALM is not prominent owing to the uniform anchored and small particle sizes of metal particles. Incorporation of the Au/Pd alloy onto ALM keeps the structure intact.

The actual microstructure, particle sizes and nature of distribution of bimetallic alloyed nanoparticles was further investigated by TEM and HRTEM analysis of representative LDH, ALM and ALM-Au/Pd samples. From the TEM image shown in Fig. 2a, LDHs are found to be composed of crystallites with typical plate-like morphology having irregular hexagonal shapes and the particle sizes within a nanometric range.³⁶ The TEM image of an ALM nanocomposite (Fig. 2b) clearly suggests the mesoporous morphology in which a good interaction exists between LDH and the framework of MCM-41 in consistence with the FTIR and N₂ adsorption-desorption study. It can be found that large quantities of small spherical bimetallic alloyed Au/Pd nanoparticles were greatly dispersed and embedded on the ALM support in a highly homogeneous manner. The corresponding particle size distribution in ALM-Au/Pd was calculated by measuring more than 200 particles from different regions. The size distribution was narrow, with an average particle size found to be about 2.5–3.5 nm (Fig. 2c and d). ALM-Au/Pd images indicate Au/Pd alloy nanostructures were encapsulated by the mesochannels of ALM nanocomposites. High-resolution TEM (HRTEM) is essential for metal nanoparticles to determine not only the shapes and particle sizes but also to give information about crystallographic phases. Moreover, when Au/Pd bimetallic nanoparticles become alloyed at any molar ratio, a face centered cubic (fcc) lattice structure arose.⁴⁵ Further, the HRTEM image (Fig. 2e) of a single alloyed NP resulted in lattice fringes with an intermediate interplanar basal spacing of about 0.230 nm, which is slightly lower than the lattice spacing of metallic Au ($d_{111} = 0.235$ nm) but higher than the metallic Pd lattice spacing ($d_{111} = 0.225$ nm). This change in interplanar lattice spacing value may result in both geometric and electronic effects, which in turn modulate the chemical and catalytic properties of the nanocomposite showing enhanced activity. These observations clearly confirm the formation of bimetallic alloyed Au/Pd nanoparticles and segregated monometallic nanoparticles with the preferentially exposed (111) plane.^{45,46} In addition, the crystal lattice spacing of 0.15 and 0.33 nm fringe corresponding to the (113) and (006) planes of LDH was observed near to Au/Pd alloy nanoparticles. The polycrystalline nature of a ALM-Au/Pd sample was confirmed by a selected-area electron diffraction (SAED) pattern (Fig. 2f). The rings are related to (006) and (110) planes of LDH with the (111) plane for the Au/Pd alloy nanoparticles in accordance with the PXRD results. Energy-dispersive X-ray (EDX) spectroscopy is one of the most useful methods for evaluating the constitution of bimetallic nanoparticles and to observe the local metal compositions and distribution of other elements. Fig. 2g represents the homogeneous dispersion of all of the elements in the ALM-Au/Pd materials.

FTIR spectra were measured to assure the existence of bonding and the influence of functional groups in the as synthesized material. Fig. 3 shows the FTIR spectra of the LDH, LM, ALM, ALM-Au, ALM-Pd and ALM-Au/Pd nanocomposites. A broad spectrum was recorded over 3300–3600

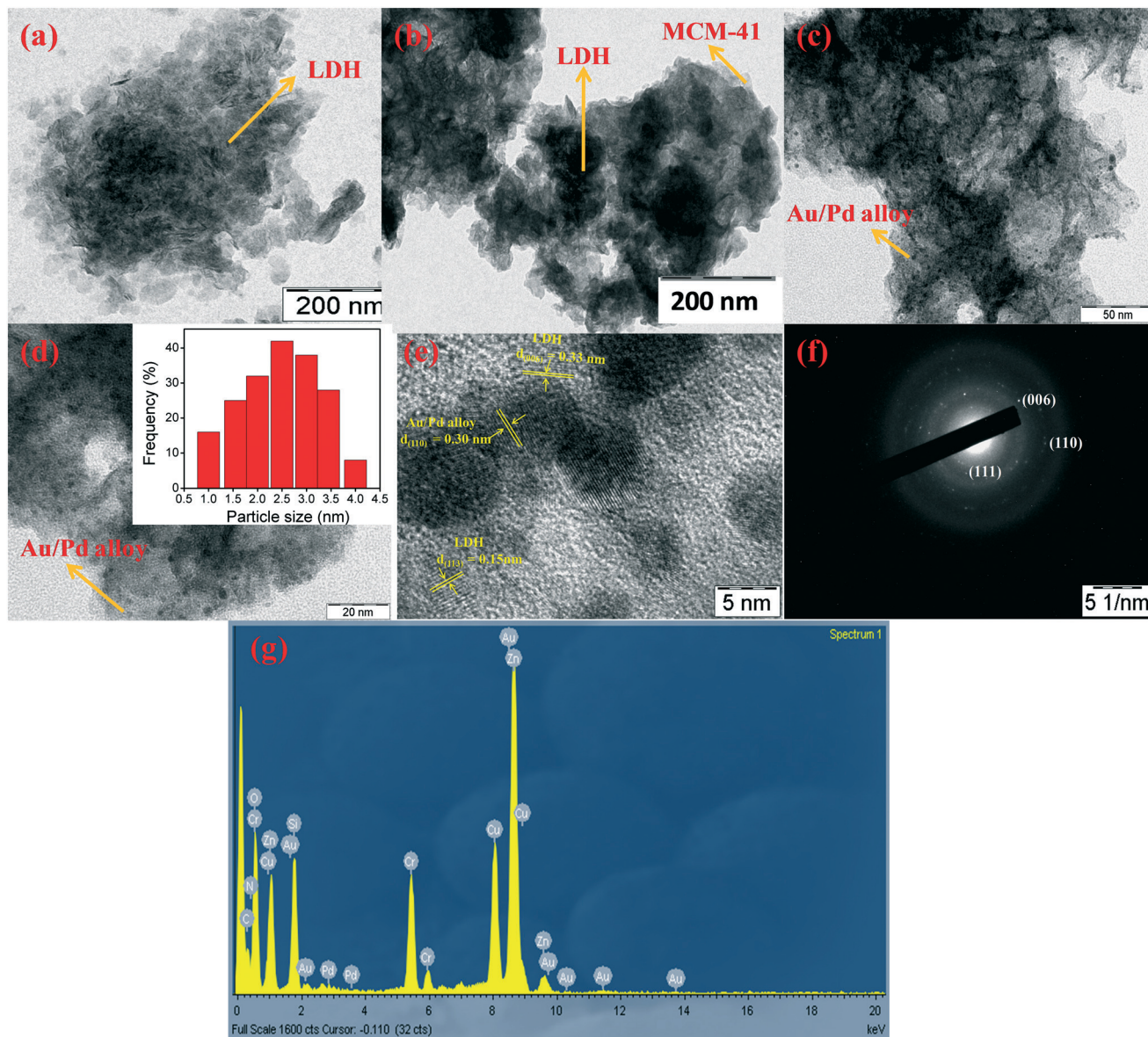


Fig. 2 TEM images of (a) LDH, (b) ALM, (c) and (d) ALM-Au/Pd. HRTEM images of (e) lattice fringes, (f) SAED pattern and (g) EDS over ALM-Au/Pd.

cm^{-1} in the case of all samples due to the stretching vibration of the $-\text{NH}_2$ group (APTES molecule), which overlapped with the surface hydroxyl groups, intercalated water molecule of LDH and also the hydroxyl group of MCM-41.^{25,37} The broadness of the peak illustrates H-bonding in a large range of vibrational frequencies. After the composite formation between LDH and MCM-41, the broadness of $-\text{NH}_2$ and $-\text{OH}$ stretching slightly decreased due to the strong interaction between APTES, LDH and MCM-41. All materials showed a weak band at $1630\text{--}1650\text{ cm}^{-1}$ for the H-O-H bending vibration of the water molecules. Whereas the symmetric and asymmetric stretching mode of carbonate anions in the inter gallery space appeared at 1493 cm^{-1} and 1370 cm^{-1} , respectively, in the case of LDH.³⁶ After composite formation, the width of the carbonate stretching vibration mode suddenly decreased because MCM-41 greatly affects the intercalated

carbonate ion which is consistent with XRD results. All the LDH based composites except MCM-41 showed a series of bands in the low frequency region due to lattice vibration and deformation modes of Zn/Cr-OH (660 cm^{-1}) and Zn-O-Cr ($585, 500\text{ cm}^{-1}$) bonds. A characteristic band at $1033\text{--}1245\text{ cm}^{-1}$ due to the Si-O stretching vibration of the Si-O-Si structure was present in the spectra of MCM-41 and all of the composites (except LDH). The existence of peaks at 966 and 790 cm^{-1} can be attributed to Si-Zn/Cr-O-Si and Si-Zn/Cr-OH vibration bands, respectively, revealing the formation of a composite between LDH and MCM-41.⁴⁷ The presence of N-H bending (750 cm^{-1}), $-\text{NH}_2$ symmetric (1532 cm^{-1}) and $-\text{CH}_2$ group asymmetric vibration (2940 cm^{-1}) of the propyl chain in APTES in the case of all composite materials (ALM, ALM-Au, ALM-Pd and ALM-Au/Pd) confirms favourable grafting of an organic moiety on the surface of ALM.⁴⁸ Even

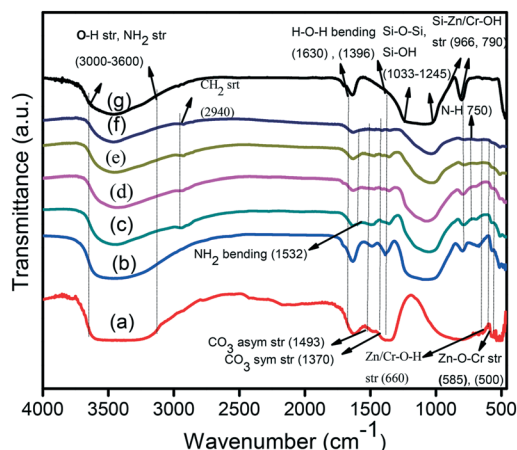


Fig. 3 FTIR spectra of (a) LDH, (b) LM, (c) ALM, (d) ALM-Pd, (e) ALM-Au, (f) ALM-Au/Pd and (g) MCM-41.

after amine functionalization and coupling with MCM-41, the corresponding vibration modes were maintained, confirming good coordination between LDH and MCM-41. After loading of noble metal nanoparticles there was no distinct variation, indicating that Au/Pd nanoparticle deposition did not alter the structure of ALM. All observed bands became sharper and clearer after loading metal nanoparticles, which was in good agreement with the PXRD analysis.

XPS is a surface responsive technique that not only gives information about the atomic composition on the surface of a catalyst but also the oxidation states regarding the binding energy of the inner shell electrons. Detailed information with respect to the bonding nature of atoms in the ALM-Au/Pd monohybrids in comparison to its pristine LDH counterpart was measured by deconvoluting XPS peaks of each element using the CASA XPS software. In the case of pure LDH, the Zn 2p and Cr 2p core lines split into four peaks of Zn 2p_{3/2} (1022.0 eV), Zn 2p_{1/2} (1045.0 eV), Cr 2p_{3/2} (577.7 eV) and Cr 2p_{1/2} (587.1 eV) shown in Fig. 4a and b, suggesting the existence of Zn(OH)₂ and Cr(OH)₃ in the positive spectra of LDH.⁴⁹ Whereas, the peaks of Zn 2p and Cr 2p in the case of the ALM-Au/Pd nanocomposite appeared at slightly higher binding energy (Zn 2p_{3/2}-1022.4 eV, Zn 2p_{1/2}-1045.5 eV, Cr 2p_{3/2}-578.1 eV and Cr 2p_{1/2}-587.6 eV) compared to pristine LDH. Additionally, the spin-orbit state of Si 2p in neat SiO₂ was observed at a binding energy of 103.2–103.7 eV, suggesting the +4 oxidation state of Si.⁵⁰ But in the present study, after composite formation with LDH and being loaded with Au/Pd alloy nanoparticles (ALM-Au/Pd), the binding energy of Si 2p was also shifted to a higher value of 103.8 eV in comparison to the reported value shown in Fig. 4e. The positive shifting in binding energies suggests reduction in the electron density around Zn, Cr, and Si in the ALM-Au/Pd due to transfer of electrons from ALM to Au/Pd alloy. As depicted in Fig. 4d, the XPS spectrum of C 1s in pure LDH showed two peaks at a binding energy of 284.9 and 288.8 eV attributed to reference carbon and carbonate anions present in the inter gallery space of the LDH structures, respectively, but in the

case of ALM-Au/Pd, three peaks from C 1s spectra were observed at binding energies of 284.9 eV, 286.5 eV and 291.5 eV for reference carbon, C–N bonding and inter gallery carbonate anions, respectively. The blue shift in the binding energy of the C 1s peak corresponding to C–N bonding and carbonate anions suggests a strong interaction exists between LDH and MCM-41. This C–N bonding peak indicates successful grafting of the APTES group on the LM surface.⁵¹ As shown in Fig. 4c, the core level peaks of the O 1s spectra in neat LDH and ALM-Au/Pd were deconvoluted. Upon deconvolution, two peaks corresponding to binding energies of 531.5 and 532.2 eV were obtained due to the hydroxide group of the brucite layer and intercalated carbonate anions in LDH, respectively.⁴⁹ After functionalisation of LM with APTES, the O 1s spectrum corresponding to a hydroxide group was shifted towards positive binding energy (531.9 eV).⁵² The increased binding energy illustrates a strong coupling of a covalent bond between –OH groups of ALM and the –OC₂H₅ group of APTES. Fig. 4f shows the N 1s spectrum of ALM-Au/Pd sample. Splitting of the N 1s spectrum into amino (–NH₂) and ammonium (–NH₃⁺) groups appeared at binding energies of 399.9 eV and 401.3 eV, respectively.⁵³ The presence of a shoulder peak from ammonium groups indicates the decrease of electron cloud density over the N atom, suggesting a chemical bond was established between Au/Pd alloy and the N atom. The amino groups have the capability to donate electrons into the transition metal owing to its electron pairs on the N atom and in other ways the Au/Pd alloy has an empty energy orbit for accepting electrons from the N atom, which results a strong coordinative bond formation between the N atom and Au/Pd alloy.²⁵

The Au 4f and Pd 3d core level spectra in the ALM-Au/Pd samples are shown in Fig. 4g and h. Four strong peaks of Au 4f (4f_{7/2} and 4f_{5/2}) and Pd 3d (3d_{5/2} and 3d_{3/2}) appeared at binding energies of 83.88 eV, 87.49 eV, 335.36 eV and 340.64 eV, respectively, in the case of the single metal loaded LDH composite.^{22,54} In contrast, after the formation of an alloy between Au and Pd in the ALM-Au/Pd nanocomposite, the binding energy of Au 4f shifted towards negative values (4f_{7/2}-83.7 eV and 4f_{5/2}-87.4 eV) whereas the spectrum of Pd 3d shifted to a higher binding energy (3d_{5/2}-335.7 eV and 3d_{3/2}-341.5 eV) relative to the monometallic reported value. This peak shifting indicates a close electronic interaction between Au and Pd in the created alloyed nanoparticles. In other words, the electron mobility takes place from the smaller electronegativity of Pd (2.2) to the larger electronegativity of Au (2.4).²⁴ That was also satisfied for formation of the Au/Pd alloy structure. Consequently, the electron cloud around the Au nucleus increases while the electron concentration decreases around the Pd nucleus.³⁴ The greater electron density leads to an increase of the screening effect of Au nanoparticles and a resulting negative shift in binding energy. A survey scan of the XPS spectra is shown in Fig. 4i. From the XPS results, it can be conclusively said that the lower binding energy of the Au/Pd alloy and higher binding energy of Zn, Cr, and Si suggests an efficient composite formation between

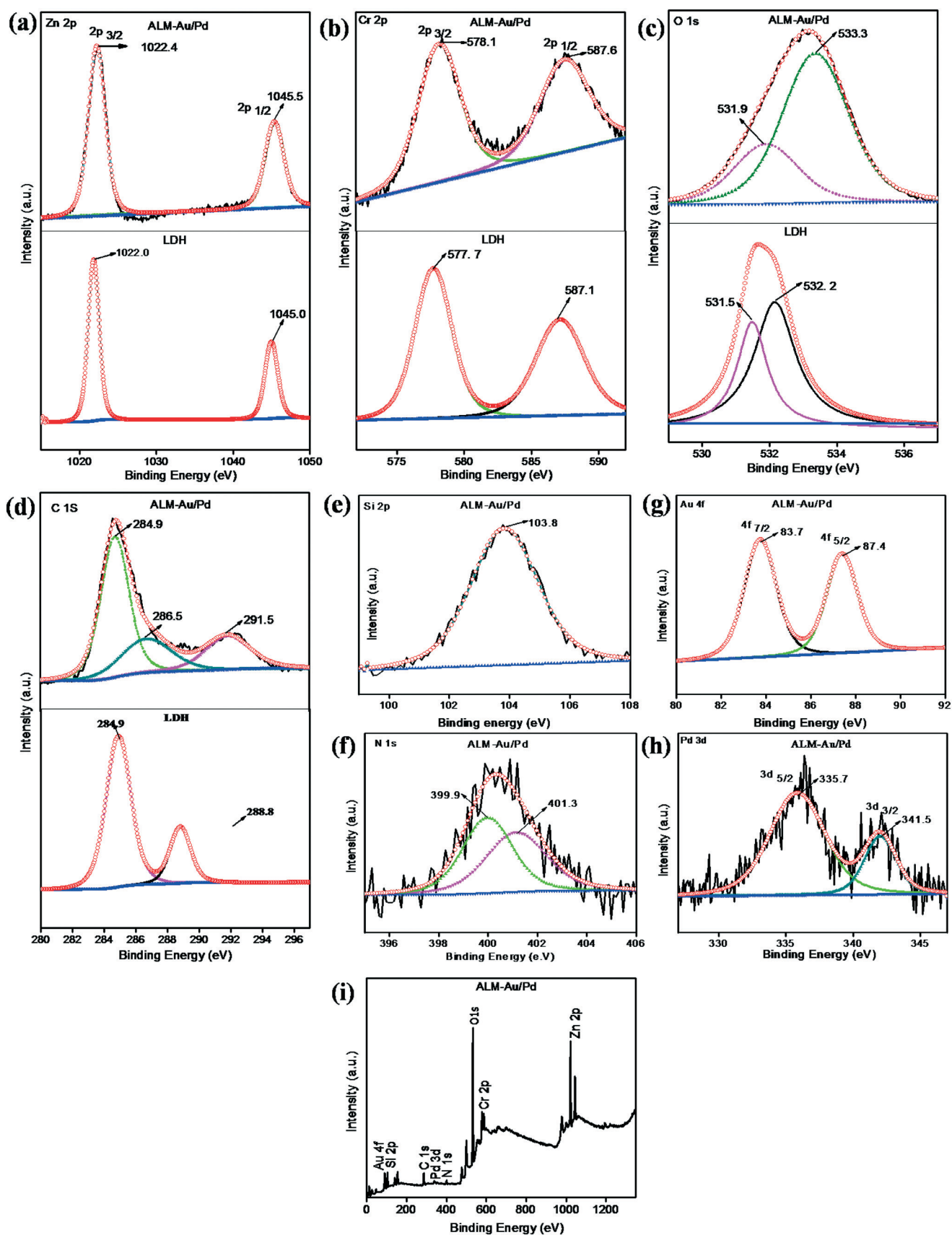


Fig. 4 High resolution deconvoluted XPS spectra of LDH and ALM-Au/Pd (a) Zn 2p, (b) Cr 2p, (c) O 1s, (d) C 1s, (e) Si 2p, (f) N1s, (g) Au 4f, (h) Pd 3d and (i) survey spectra.

ALM and Au/Pd alloy nanoparticles in which the charge heterogeneity on the alloy's surface enhanced the photocatalytic organic conversion process.

The opto-electronic behaviours of the as prepared samples were analysed by UV-visible absorption spectrum and represented in Fig. 5. It was seen that, after the formation of ALM and after loading noble metal nanoparticles, the absorption edge shifted towards a longer wavelength, indicating enhanced light absorption and consequently improved photocatalytic activity in the visible region. The absorption edge of LDH gradually increased towards higher wavelengths with loading of monometallic noble metal nanoparticles to bimetallic alloyed noble metal nanoparticles. Neat LDH showed an intrinsic optical band was located in the UV zone owing to the ligand-metal charge transfer spectra (LMCT) taking place from the transition from the O 2p orbital to Zn 4s and Cr 3d orbitals. Other absorption bands in the 270–320 nm regions were due to ligand to metal charge transfer (LMCT) from the O-2p orbital to the Zn-4s and Cr-3d orbital. In the visible light region, the absorption peaks at 413 and 570 nm are attributed to the $4A_2g \rightarrow 4T_1g(F)$ and $4A_2g \rightarrow 4T_2g(F)$ d-d transitions of the Cr^{3+} ions, respectively.⁵⁵ After loading of Au nanoparticles, ALM-Au should show a LSPR peak around 520 nm, however, in this case a broad absorption peak appeared as the LSPR peak overlapped with the MMCT band of ALM. Moreover, upon loading Pd nanoparticles the LSPR band of the Au nanoparticles changed and a broad weak characteristic peak was observed at about 520–570 nm (ALM-Au/Pd).²² The combination of Au atoms with Pd atoms resulted in a change in the colour of the sample from purple to gray. It has been reported that incorporation of Pd into the crystal lattice of Au changes the crystal structure of Au; this phenomenon was based on previous observations, that the presence of a metal atom (group 10) with d^8s^2 configuration in bimetallic alloyed nanoparticles suppresses the LSPR energy of a metal atom (group 10) with $d^{10}s^2$ configuration.⁴¹ The band-gap energy of LDH can be calculated by fitting the absorption data with the Kubelka-Munk equation and Tauc's plot (Fig.

S2†). The neat LDH displayed directly allowed transitions and band-gap energy values found to be 2.5. This band gap of LDH indicates ability of harvesting visible light photons.⁵⁶

Photocatalytic activity towards the one-pot synthesis of imine from benzyl alcohol and nitrobenzene

First, the photocatalytic activities of the amine functionalised materials ($AL_{0.2}M$, $AL_{0.33}M$, $AL_{0.5}M$ and ALM) were completed for selective photoconversion of benzyl alcohol to benzaldehyde under visible light irradiation ($\lambda \geq 420$ nm) (Table S1†). ALM (weight ratio between LDH to MCM-41 is 1:1) showed better conversion efficiency of benzyl alcohol (48.7%) with higher yield (46%) and selectivity (88%) compared to other materials due to the higher concentration of LDH which makes available a large number of active sites for a photocatalytic reaction. To again improve the photocatalytic organic conversion of ALM photocatalysts, mono metal (Au, Pd) and bimetal (Au/Pd), nanoparticles were loaded into it. Fig. 6a represents benzyl alcohol conversion, yield and selectivity towards benzaldehyde over all the prepared samples (MCM-41, LDH, ALM, ALM-Au, ALM-Pd and ALM-Au/Pd). It was clearly seen that the rate of conversion and yield increased from MCM-41 to the ALM-Au/Pd nanocomposite. For pure MCM-41, a low rate of conversion (10.3%) and yield (8%) was achieved. The conversion and yield were found to be 42% and 40%, respectively, in the case of pure LDH. After functionalisation of APTES on the LM composite, the yield and conversion increased to 46% and 48.7%, respectively. Furthermore, noble metal loading enhanced the photoconversion ability of LDH. The ALM-Pd (66% yield) and ALM-Au (76.2% yield) showed conversions of 68.9% and 81%, respectively. The loading of bimetal significantly increased the conversion and yield over individual monometal nanocomposites and parent catalysts. ALM-Au/Pd showed the highest conversion (92%) and yield (90%) of benzyl alcohol to benzaldehyde. The selectivity of the oxidative product over all catalysts (except MCM-41) was higher than 85%.

A tandem photocatalytic reaction was carried out for the synthesis of imine from benzyl alcohol and nitrobenzene conversion over all samples under visible light illumination ($\lambda \geq 420$ nm). As shown in Fig. 6b, pure MCM-41 showed a negligible yield of imine (3.9%) with less conversion of benzyl alcohol and nitrobenzene than all other catalysts owing to its non-sensitive light response.³⁷ In bare LDH, the yields of imine were very low (22%), the benzyl alcohol (48%) and nitrobenzene (53.1%) conversions were also insignificant which suggests that LDH is a less active material for imine synthesis due to its low capacity of photoinduced charge pair separation. Reactants and intermediates formed during the condensation may also block the active sites of LDH. The ALM nanocomposite converted almost half of benzyl alcohol (56.3%) and nitrobenzene (62.8%), but their imine yield was only 31%. This indicates condensation of benzaldehyde with aniline did not occur efficiently on the ALM surface. The imine yield over all catalysts is depicted in the following sequence:

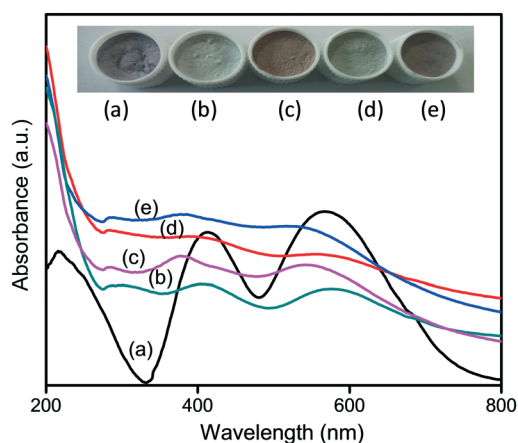


Fig. 5 UV-vis diffuse reflectance spectra of (a) LDH, (b) ALM, (c) ALM-Au, (d) ALM-Pd and (e) ALM-Au/Pd.

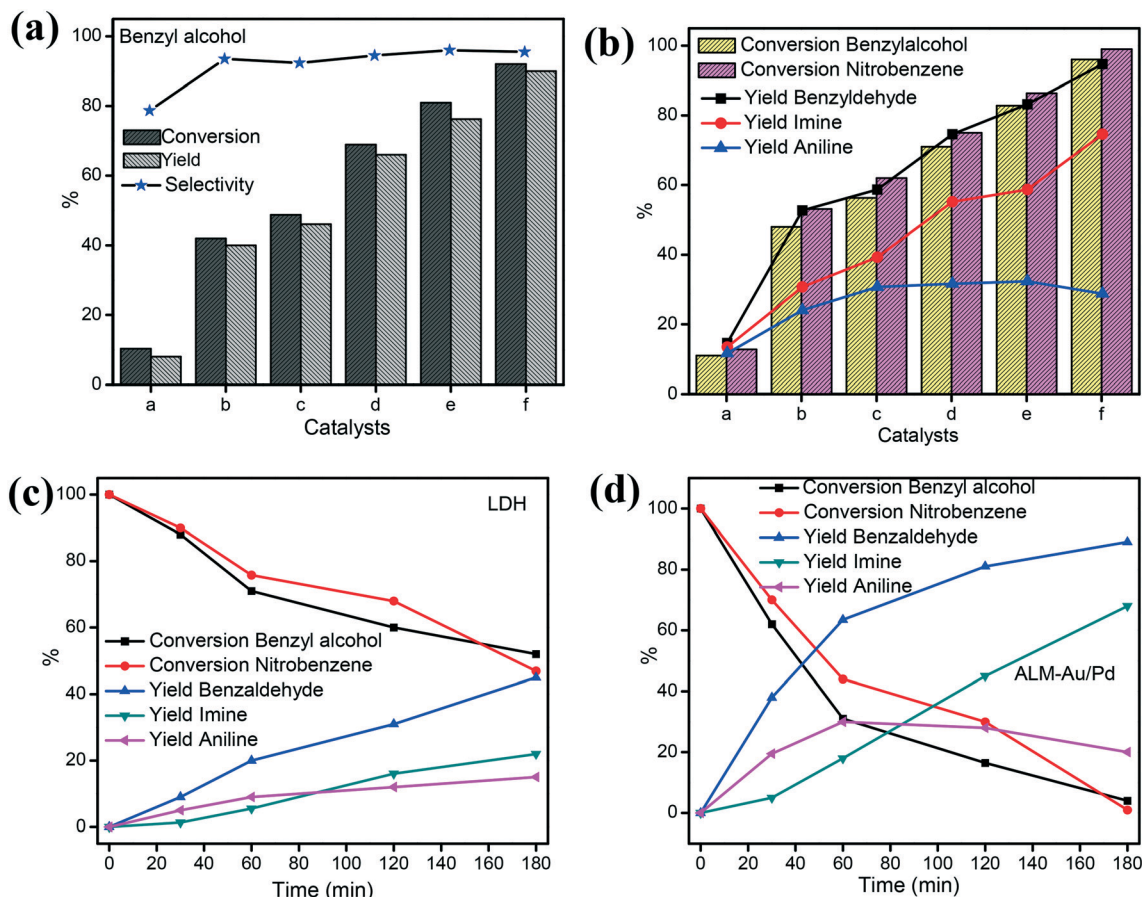


Fig. 6 (a) Photocatalytic benzyl alcohol oxidation of as prepared catalysts [(a) MCM-41 (b) LDH (c) ALM (d) ALM-Pd (e) ALM-Au and (f) ALM-Au/Pd], (b) photocatalytic one-pot imine synthesis from benzyl alcohol and nitrobenzene [(a) MCM-41, (b) LDH, (c) ALM, (d) ALM-Pd (e) ALM-Au, and (f) ALM-Au/Pd]. Time-dependent changes in the reactant and product amounts during the photoconversion of benzyl alcohol and nitrobenzene with (c) LDH and (d) ALM-Au/Pd.

MCM-41 (3.9%) < LDH (22%) < ALM (31%) < ALM-Pd (47.6%) < ALM-Au (51.3%) < ALM-Au/Pd (68%). The introduction of noble metal onto the ALM surface enhanced the photoconversion activity. The plasmonic metal nanoparticles possess a LSPR effect and efficiently harvest photon energy owing to its intense and broad absorption spectra over the whole visible spectrum. The sample ALM-Au/Pd nanocomposite promoted complete reaction of nitrobenzene (99%) and benzyl alcohol (96%) with a very high yield and selectivity of imine than the monometal composite. Upon alloy formation between Au and Pd, the charge distribution that takes place between these two metal leads to development of a surface electronic heterogeneity which enhances the interaction between organic substrates and the alloy's surface.¹³ This facilitates more active sites for an improved photocatalytic organic conversion reaction. The synergetic interaction between Au/Pd alloy nanostructure and ALM nanocomposite enhances the production of imine which proceeds energetically by the successive coupling of the photo-produced benzaldehyde and aniline on the ALM-Au/Pd surface. Fig. 6a, b and Table S2[†] represent the conversions, yields and selectivities of all reactants and products from all samples. To get more information about im-

ine synthesis, the reaction also was carried out under dark conditions. As shown in Fig. S3,[†] a negligible amount of yield (imine) was obtained from all the catalysts. This indicates that the one-pot condensation reaction of benzyl alcohol and nitrobenzene over the ALM-Au/Pd was a photocatalytic process.

Fig. 6b and c summarize the time-dependent changes in the amounts of reactants and products during the photocatalytic one-pot condensation reaction with LDH and ALM-Au/Pd. In the first stage, benzaldehyde and aniline were obtained, along with reduction in the concentrations of benzyl alcohol and nitrobenzene. With an increase in the light illumination time, the amount of aniline gradually increased up to 1 h. After 1 h, the imine formation improved while reducing the aniline quantity. Subsequently after 3 h of light irradiation, approximately a maximum amount of nitrobenzene (99%) was converted to imine (68%), with the generation of benzaldehyde. This is fully in agreement with the following eqn (8)–(12). The photocatalytic one-pot synthesis of imines is quite impressive over an ALM-Au/Pd nanocomposite. In less time, a high yield of imine was obtained compared to other semiconductor-based photocatalysts, as documented in Table 2.

Table 2 Photocatalytic one-pot imine synthesis over different catalysts

Photocatalysts	Substrates	Yield of product (imine)	Reaction conditions	Ref.
CdS(15%)-TiO ₂	Benzyl alcohol (150 μmol), nitrobenzene (50 μmol)	>99%	Catalyst (10 mg), solvent (hexane 5.0 mL), blue LED light, ($\lambda > 420$ nm) at room temperature, N ₂ , time: 12 h	57
P25 TiO ₂	Benzyl alcohol (5 mL), nitrobenzene (0.05 mmol)	92%	Catalyst (5 mg), 2 kW Xe lamp ($\lambda > 300$ nm), at room temperature, N ₂ , time: 10 h	7
Pt(0.3)@TiO ₂	Benzyl alcohol (5 mL), aniline (10 mmol)	97%	Catalyst (5 mg), light ($\lambda > 300$ nm), at room temperature, N ₂ , time: 12 h	58
Cd _{0.78} Zn _{0.22} S	Benzyl alcohol (2.55 mol L ⁻¹), nitrobenzene (8.5 mol L ⁻¹)	36.8%	Catalyst (80 mg) solvent (BTF, 15 mL), 300 wt xenon lamp ($\lambda > 420$ nm), at 50 °C, N ₂ , time: 2 h	35
ALM-Au/Pd (present research)	Benzyl alcohol (3 mmol), nitrobenzene (1 mmol)	68%	Catalyst (50 mg) solvent (acetonitrile, 10 mL), 250 wt medium pressure Hg lamp ($\lambda \geq 420$ nm), time: 3 h	

Evidence in support of a mechanistic approach for enhanced photocatalytic organic conversion over the ALM-Au/Pd nanocomposite

PL spectroscopy is a powerful and non-destructive technique for elucidating the radiative recombination of charge carriers and characterising the quality of semiconducting materials. The PL emission peak is useful for quantifying the impurity content of a material, optical emission efficiencies, composition of the material (alloy composition), and gives an idea about localized defect levels generated in a semiconducting

material. Fig. 7a represents (LDH was inserted) the PL emission spectra of all synthesized materials under an excitation wave length of 350 nm. A strong emission peak at 430–450 nm was observed from the radiative recombination of localized surface trapped charge pairs of LDH. The presence of a weak band at 470 nm corresponds to the band-to-band emission peak of LDH. Moreover, the less intense peaks at about 500 nm may be due to surface defect sites in the material.⁵⁵ There is a drastic decrease in PL intensity in the case of the bimetallic alloyed ALM composite in comparison to neat LDH, ALM and monometallic composites indicating a

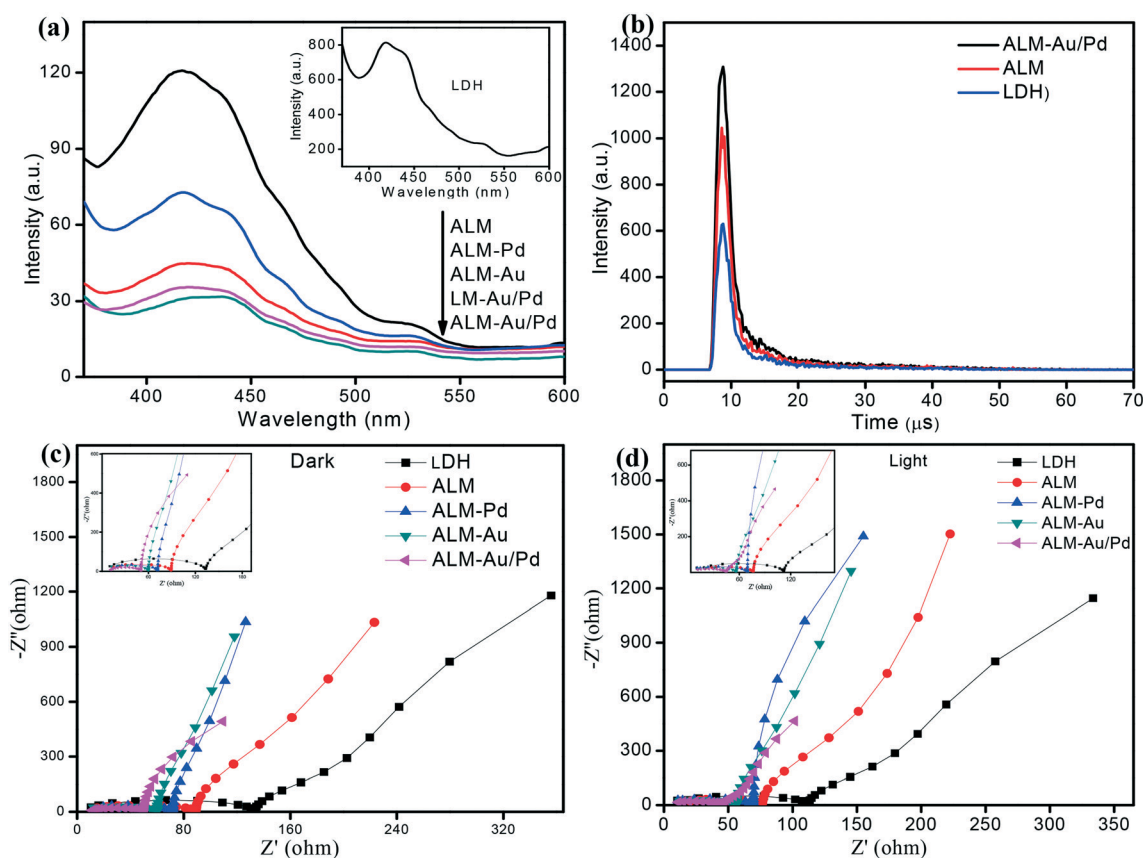


Fig. 7 (a) PL spectra of all samples (excludes MCM-41), (b) TRPL spectra of LDH, ALM and ALM-Au/Pd and (c and d) EIS spectra of LDH, ALM, ALM-Pd, ALM-Au and ALM-Au/Pd under dark and light irradiation conditions.

significant depression of electron–hole recombination. Generally, a reduced PL intensity usually suggests a better separation and transportation efficiency of photoinduced charge carriers. The Au/Pd alloy heterostructure on the ALM surface successfully inhibits the recombination rate of photoinduced charge pairs of LDH by the effect of efficient charge migration which is in good agreement with the photocatalytic activity. Furthermore, in contrast to the Au/Pd loaded without amine functionalised LM nanocomposite (LM–Au/Pd), a reduced PL intensity is also observed for the ALM–Au/Pd photocatalyst indicating the separation and transfer of charge carriers through interfaces formed by chemical bonding between ALM and Au/Pd alloy nanoparticles was more proficient. It was observed that after functionalisation, the APTES group in spite of hindering the electron–hole separation process in ALM–Au/Pd photocatalyst, favoured good dispersion of Au/Pd alloy nanoparticles on the ALM's surface and provided a good number of active sites for photo catalytic reactions.

Furthermore, to explain the possible charge transfer dynamics, a TRPL study of the samples (LDH, ALM and ALM–Au/Pd) was carried out, as displayed in Fig. 8b. TRPL spectroscopy helps to describe the increase in the lifetimes of the charge carriers in a ALM–Au/Pd nanocomposite and decay times of the pure LDH and ALM samples. The different charge pair recombination mechanisms are a function of different PL decay lifetimes of the photocatalysts. The TRPL of the samples

was carried out at an excitation wavelength of 350 nm. The depicted plots were fitted with bi-exponential decay functions as expressed by the following equation (eqn (5)):⁵⁹

$$I(t) = A_1 e^{-\frac{t}{\tau_1}} + A_2 e^{-\frac{t}{\tau_2}} \quad (5)$$

where τ_1 and τ_2 ($\tau_1 < \tau_2$) are represented by two decay lifetimes of faster and slower components, respectively, and the corresponding A_1 and A_2 are the PL amplitudes. The τ_1 originates due to direct generation of charge pairs and τ_2 initiates from the direct formation of self-quenched excitation electrons. The average intensity lifetimes of both materials were estimated by making an overall comparison of the emission decay behaviour. The average lifetime (τ) was determined from the following equation (eqn (6)):

$$\tau = \frac{A_1 \tau_1^2 + A_2 \tau_2^2}{A_1 \tau_1 + A_2 \tau_2} \quad (6)$$

The bi-exponential decay kinetics are associated with defect level emission from a charge pair recombination of localized excitation. The calculated average life times of LDH (10.6 μ s), ALM (14.6 μ s) and ALM–Au/Pd (16.2 μ s) are shown in Table 3. An increased average life time in the case of the

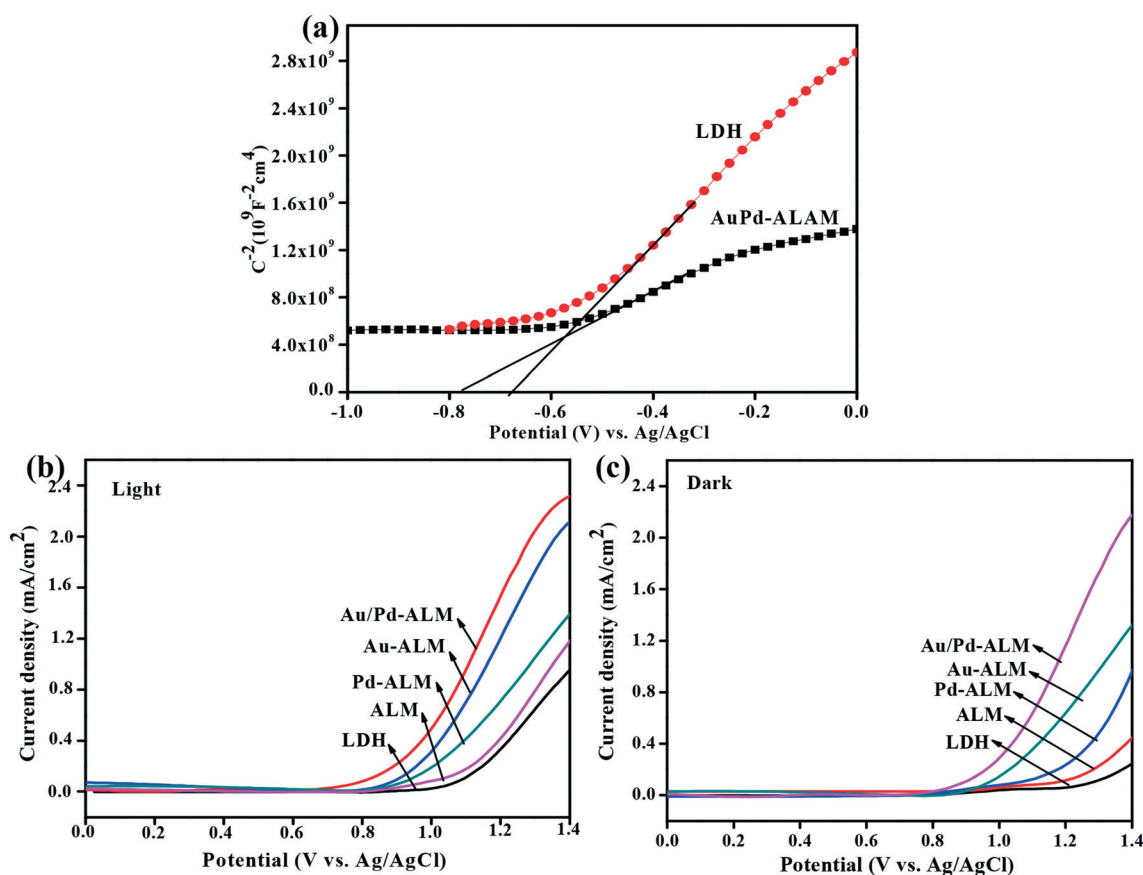


Fig. 8 (a) MS plot of LDH and ALM–Au/Pd, (b) LSV curves of all of the photocatalysts under light illumination and (c) dark conditions.

Table 3 Photoinduced charge lifetimes of LDH, ALM and ALM–Au/Pd materials

Catalysts	A_1 (%)	τ_1 (μ s)	A_2 (%)	τ_2 (μ s)	τ (μ s)
LDH	10.09	1.20	89.90	10.69	10.6
ALM	8.71	1.4	91.28	14.66	14.6
ALM–Au/Pd	8.46	1.51	91.53	16.32	16.20

ALM–Au/Pd nanocomposite suggests efficient transfer of a photo excited electron–hole between Au/Pd alloys to ALM with decreasing radiative recombination. This indicates a reduction in the recombination probability of localised excitation and subsequently a larger number of photo induced electrons and holes are made available to participate in photocatalytic organic conversion reactions.

Further to explore the electrode/electrolyte reaction kinetics and the interfacial charge transfer process, EIS of all of the synthesised catalysts was carried out both under dark and light conditions. In the photocatalytic process, the interfacial charge separation ability of the photoinduced charge carriers is an important factor and it can be measured by an EIS Nyquist plot. The resulting Nyquist plots as displayed in Fig. 7c and d were found to consist of a primary semi-circular portion to examine the charge transfer resistance. A smaller diameter of an impedance arc indicates lower charge transfer resistance offered by the electrode and so the conductivity is higher. It was evident that, as shown in Fig. 7c and d, the diameters of all of the prepared electrodes were considerably greater under dark conditions than those under visible light irradiation, thus representing a larger resistance in the former case, which allowed only a few charge migrations. Under the illumination of visible light, the impedance reduced significantly due to the formation of plentiful photogenerated charge pairs. In the case of both dark and light irradiation conditions the order of resistance followed the same trend, which was: LDH (dark-133 Ω , light-112 Ω) < ALM (dark-89 Ω , light-77 Ω) < ALM–Pd (dark-72 Ω , light-68 Ω), < ALM–Pd (dark-59 Ω , light-56 Ω) < ALM–Au/Pd (dark-50 Ω light-44 Ω). Apparently, the decreasing trend in the diameters of the semicircles explains the greatly enhanced photocatalytic activity of ALM–Au/Pd. After loading Au/Pd alloy nanoparticles as the solution/electrolyte resistance decreased, the conductivity increased effectively to support this activity. Actually, the smallest arc was from the ALM–Au/Pd nanocomposite, which suggests that the developed surface charge heterogeneity on the Au/Pd alloy surface retards the high interfacial charge transfer resistance, resulting in the rich electronic and ionic conductivities of this material. The linear portion in the Nyquist plot is the Warburg impedance (Ws) which represents the ion diffusion process in the electrolyte supporting the photocurrent response.⁶⁰ The lowest Warburg impedance was in the case of ALM–Au/Pd under dark and visible light illumination in comparison to neat counterparts and the monometal nanocomposite confirmed effective ion diffusion, in good agreement with the photocatalytic organic transformation.

Based on the results of the steady state PL spectra, TRPL and EIS measurements, it can be concluded that the modification of a small amount of Au/Pd alloy on the ALM surface can efficiently separate the recombination properties of photo induced charge carriers in ALM and effectively accelerate visible light conversion efficiency. This is why the ALM–Au/Pd nanocomposite showed the best photo organic transformation activity.

Photoelectrochemical study

Mott–Schottky plots were drawn to study the electronic structure, semiconducting nature and underlying mechanism of the photocatalytic reaction. As displayed in Fig. 8a, both LDH and ALM–Au/Pd show positive slopes in the Mott–Schottky plots ($1/C^2$ versus the electrode potential), which correspond to an overall shape consistent with typical n-type semiconductors with electrons as the major charge carrier. The flat band potential (V_{fb}) can be calculated from the X-intercept obtained by extrapolating the linear portion of the M–S plot by using equation (eqn (7)).⁶¹

$$\frac{1}{C^2} = \left(\frac{2}{q\epsilon_0\epsilon N_d} \right) \left(V_{app} - V_{FB} - \frac{kT}{q} \right) \quad (7)$$

where, N_d is the donor density, V_{app} is the applied potential, ϵ is the dielectric constant, ϵ_0 is the permittivity of the vacuum and kT/q represents the temperature dependence term. And $1/C^2 = 0$, gives the V_{FB} (flat band potential) vs. Ag/AgCl electrode. The flat band potential of LDH was obtained as -0.68 V vs. the Ag/AgCl reference electrode (-0.08 V vs. NHE). Generally for an n-type semiconducting material, the flat band potential is situated near to its conduction band (CB) potential.⁶² Therefore, the CB edge of LDH was found to be -0.08 V vs. NHE and from the Tauc plot, the band gap energy of LDH was found to be 2.5 eV, so the valence band (VB) potential of LDH was determined to be 2.42 V vs. NHE. Moreover, the smaller slope of Au/Pd–ALM compared to that of LDH represents a higher carrier density as well as highest donor density in the composite, which is beneficial for improved electronic conductivity within the photoanode to support efficient electron–hole separation. The slight negative shift in the flat band potential was from -0.68 V for LDH to -0.76 V in the case of Au/Pd–ALM. This negative shift in the flat band potential may be attributed to band unpinning with surface trapped holes, representing efficient electrode/electrolyte interface charge transfer, resulting in an upward shift in the Fermi level by increasing the degree of band bending and deeply enhances the efficiency of photogenerated charge carriers separation and migration.⁶³

The photoelectrochemical activities of LDH, ALM, ALM–Au, ALM–Pd and ALM–Au/Pd photoelectrodes were investigated from their polarization curves by LSV. As shown in Fig. 8b and c, all of the photoelectrodes displayed anodic

photocurrents owing to their n-type conductivity under visible light illumination and dark conditions. It was observed that all of the neat materials show comparatively small anodic current response in the applied potential window, thus signifying poor photocatalytic behaviour compared to the metal incorporated samples. However, upon integrating MCM-41 with LDH and loading it with noble metal nanoparticles, the photoelectrocatalytic performance of the composite significantly increased both in the dark and in the presence of light. Upon visible light irradiation, all of the photocatalysts exhibited higher photocurrent density than in dark conditions. The LDH, ALM, ALM-Au, ALM-Pd and ALM-Au/Pd photoelectrodes showed anodic photocurrent densities of 2.3, 2.0, 1.4, 1.1 and 0.9 mA cm⁻² in the region of 0 to 1.4 V, respectively, with successive cathodic shifts in the onset potential under the illumination of visible light. The improved photocurrent density of ALM-Au/Pd suggests that the Au/Pd alloy heterostructure can efficiently accelerate the photon harvesting capability and photoconversion activity of LDH. The synergistic effect of Au/Pd alloyed nanostructure and charge heterogeneity encourages fast separation of the photogenerated charge carrier. The faster transfer rate of photoinduced charge carriers improved electron-hole separation efficiency and also increased the photocurrent. This enhanced activity was due to new active sites and the Schottky barrier generated at the Au/Pd nanoparticle-semiconductor interface that facilitates the surface redox reaction.⁶⁴ Under light illumination, the excited electrons could readily migrate and diffuse easily, resulting in a higher anodic current. Hence, the enhanced photoconversion activity was attributed to the synergistic effect of the co-doped Au/Pd nanoalloy in increasing electron shuttling, which accelerated the fast transport and separation of the photogenerated charge carrier along with the lower resistance offered by the photocatalyst. Moreover, the efficiency of charge carrier separation in ALM-Au/Pd also was evidenced by the PL study.

Scavenger study for photocatalytic conversion

To explain the photocatalytic charge transfer mechanism, detection of the active species was very important. In a nitrogen atmosphere, photogenerated electrons (e⁻) and holes (h⁺) are the most important reductive and oxidative reactive species for a selective redox organic transformation reaction.³⁵ A control experiment was conducted over the ALM-Au/Pd nanocomposite in order to determine the effects of photoexcited h⁺ and e⁻ on the selective synthesis of imine in the coupled photocatalytic system of benzyl alcohol oxidation and nitrobenzene reduction. In this experiment, AgNO₃ and TEA were used as electron and hole scavengers, respectively. As shown in Fig. 9, when TEA was introduced into the reaction system, the yield of all three products was significantly reduced from 89.6% to 40%, 20% to 8% and 68% to 16.3% for benzaldehyde, aniline and imine, respectively. The decreased yield of benzaldehyde indicates that h⁺ is the reactive species for selective photooxidation of benzyl alcohol. In general, when

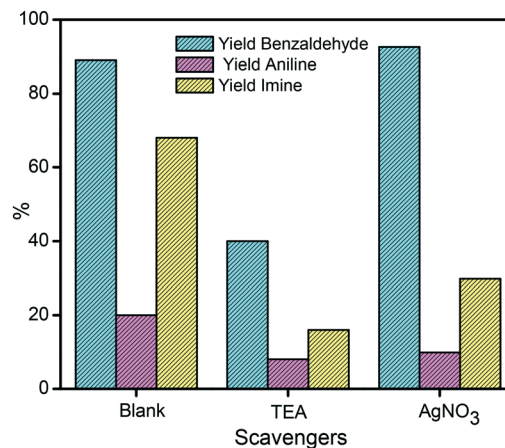
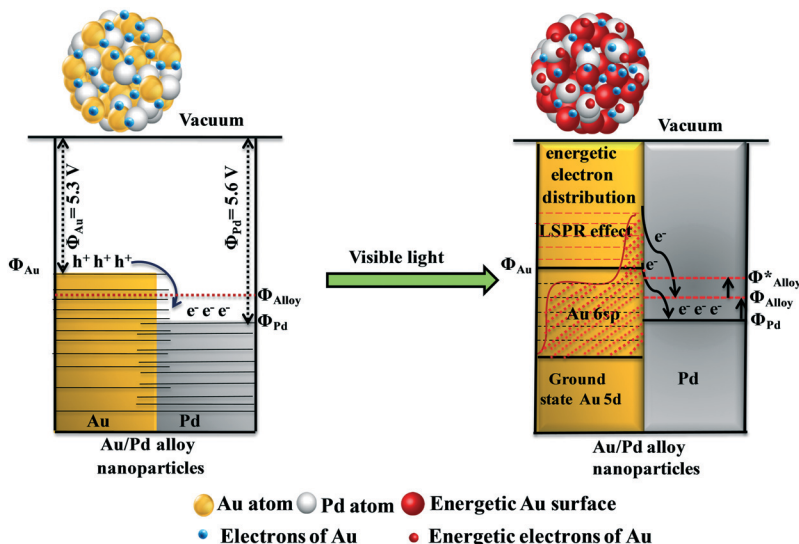


Fig. 9 Benzyl alcohol and nitrobenzene conversion rates over ALM-Au/Pd in the presence of various radical scavengers.

photogenerated holes are quenched in a reaction process, the recombination of charge pairs is hindered and the corresponding photoinduced electrons are available for the reduction reaction. But, in the present system, the lower yield of aniline compared to the control experiment suggests the reduction of nitrobenzene depends on the oxidation of benzyl alcohol. This may be due to those protons (H⁺) generated during the photooxidation of benzyl alcohol which are responsible for the reduction of nitrobenzene into aniline. Moreover, a lower yield of benzaldehyde and aniline could not produce more imine. However, with the addition of AgNO₃ as an e⁻ scavenger, the yields of imine (29.8%) and aniline (9.9%) remarkably decreased, but the benzaldehyde quantity was slightly enhanced from 89% to 90.4%. From the above quenching experiments, it was concluded that the photoinduced h⁺ and e⁻ are decisive factors in the imine synthesis through photocatalytic conversion of benzyl alcohol and nitrobenzene, respectively.

Imine synthesis through a photocatalytic charge transfer mechanism

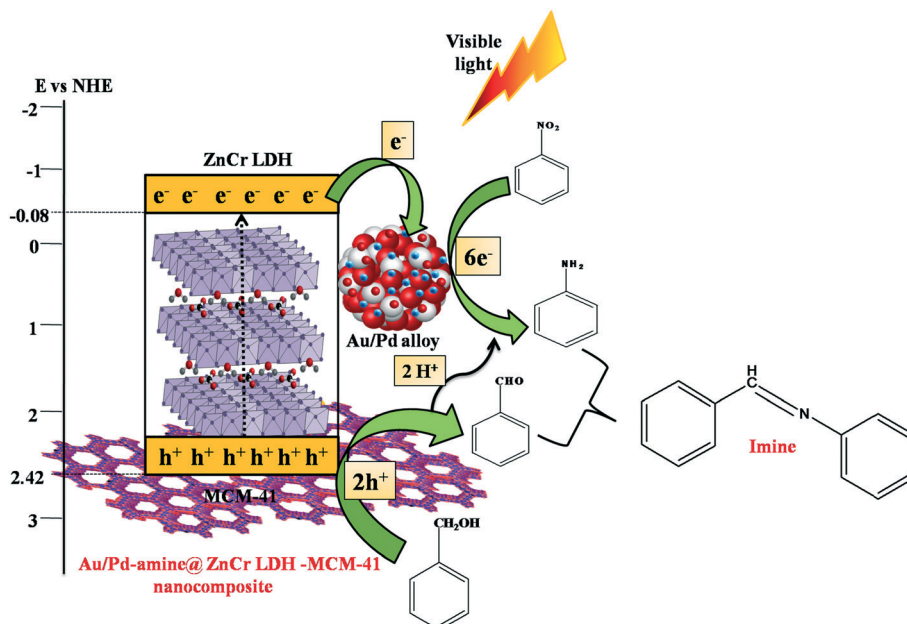
Based on the above results and discussion, a possible mechanism for imine formation *via* tandem photocatalytic conversion of benzyl alcohol and nitrobenzene followed by coupling between benzaldehyde and aniline over ALM-Au/Pd photocatalyst was proposed (Scheme 3). The proposed photocatalytic mechanism explains the synergistic effect between the Au/Pd alloy nanostructure and LDH in the ALM-Au/Pd nanocomposite. The imine synthesis was first achieved by oxidation of benzyl alcohol followed by reduction of nitrobenzene. When ALM-Au/Pd is irradiated and excited by visible photons, the electrons of VB are excited in the CB of LDH and then rapidly transferred to Au/Pd alloy sites as the Au/Pd bimetallic alloy has a higher electron-capturing tendency due to its low lying Fermi level.¹⁴ This electron migration could result in the creation of a metal-semiconductor Schottky junction, which can efficiently trap the photogenerated



Scheme 2 The impact of alloying with visible light illumination of the Au/Pd alloy nanoparticles [surface electronic behaviour of the Au/Pd alloy nanoparticles is unlike those of single Au and Pd nanoparticles. The Pd sites have more electron density than Au sites because Pd has a slightly greater work function ($\phi_{\text{Pd}} = 5.6$) than Au ($\phi_{\text{Au}} = 5.3$). To maintain the Fermi level equilibrium, electrons will move from Au to the Pd site and consequently, the electronic chemical gradient between the two metals is equal (ϕ_{alloy}). After light absorption by Au nanoparticles in the Au/Pd alloy, the resulting energetic electrons (hot electrons) are transferred from Au to Pd. The Fermi level of alloy nanoparticles without light illumination is lower than under light illumination (ϕ_{alloy}^*).

electrons and assist electron–hole separation, thus accelerating the photocatalytic activity. In addition, upon visible light irradiation, the photons were absorbed by Au/Pd alloyed nanoparticles through LSPR excitation, resulting in hot electrons on the alloy surface. Subsequently, the hot electrons of Au and photogenerated electrons of LDH together transferred to the Pd site. As depicted in Scheme 2, the work function ($\phi_{\text{Pd}} = 5.6$) of Pd is a little larger than the work function

of Au ($\phi_{\text{Au}} = 5.3$). Under visible light illumination in the alloyed nanostructure, when the two metals are in contact with each other, in order to achieve equilibrium (ϕ_{alloy}^*) the energetic electrons will flow from Au to Pd to establish an equal chemical potential gradient. Owing to this charge redistribution, the Pd atom becomes rich in electrons and the Au atom electronically deficient. This heterogeneity in charge distribution enhanced the interactions between reactant



Scheme 3 Photocatalytic one-pot imine synthesis mechanism from benzyl alcohol and nitrobenzene over the ALM–Au/Pd nanocomposite.

molecules (benzyl alcohol and nitrobenzene) and Au/Pd alloy nanoparticles, independent of the electrophilic/nucleophilic nature of the reactants. The close interaction leads to a decrease in the activation energy and ultimately increases the rate of the photocatalytic reaction. At the same time, the positively charged photogenerated holes could accumulate in the VB of LDH. The Brønsted and Lewis surface basic sites of ALM-Au/Pd help to facilitate the deprotonation of surface adsorbed benzyl alcohol and to form alkoxide anions. Then alkoxide anions react with the photogenerated holes at VB of LDH to form carbon radicals by releasing another H^+ . The obtained carbon radicals further react with photogenerated holes to form benzaldehyde. Subsequently, electrons gather at the Au/Pd bimetallic alloy nanoparticles and the presence of H^+ generated during oxidation process could efficiently react with nitrobenzene to form nitrosobenzene and H_2O molecules. After that, the nitrosobenzene gradually converts to aniline as the reaction progresses. Finally, benzaldehyde couples with aniline to produce imine by discharging water. The released hydrogens during the conversion of benzyl

alcohol to benzaldehyde are mainly hydroxyl hydrogens and α -hydrogens of benzyl alcohol, respectively, and the imine hydrogen is initiated from benzaldehyde. This organic transformation reaction indicates that the photocatalytic oxidation of benzyl alcohol to benzaldehyde involves 2 photogenerated holes and the photocatalytic reduction of nitrobenzene to aniline requires 6 electrons and 6 protons (H^+). This 6 mol of protons are generated from 3 mol of benzyl alcohol. Therefore, according to theoretical calculations, the amount of benzyl alcohol should be three times that of nitrobenzene. Moreover, 1 mol of imine is produced by the condensation reaction between 1 mol of benzaldehyde and 1 mol of aniline.^{35,65} So, after completion of the tandem reaction, the concentration of the produced benzaldehyde should be two times that of imine. The detailed photocatalytic organic reaction mechanism can be explained by the following equations (eqn (8)–(12)). Thus, it is made clear that the formation of imine was definitely synthesized from benzyl alcohol and nitrobenzene in the current photocatalytic reaction system.

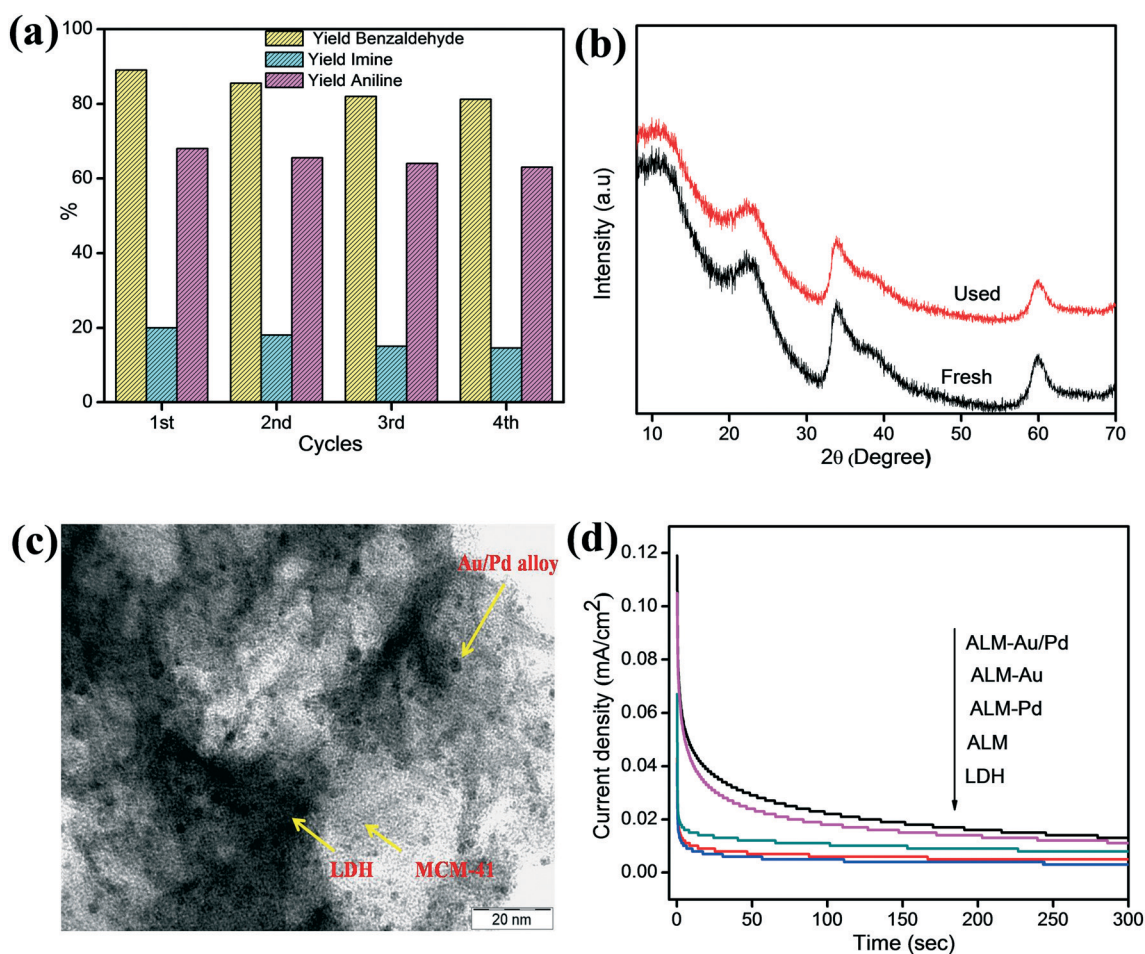
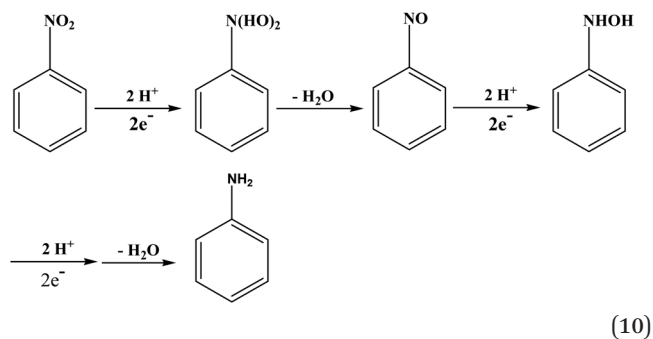
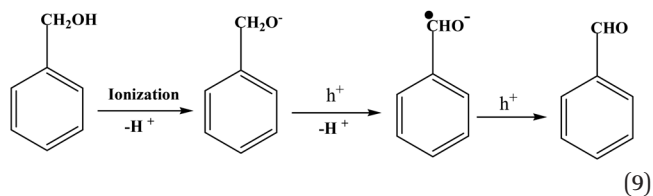
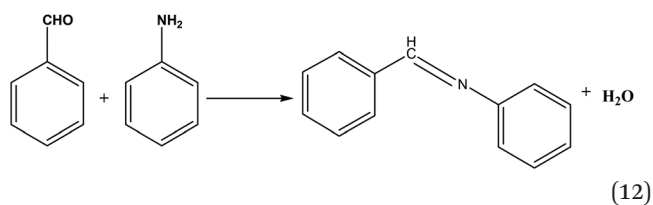
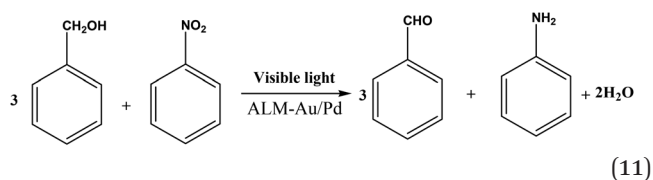


Fig. 10 Reusability study of (a) imine synthesis in four consecutive cycles of running every 3 h for the ALM-Au/Pd nanocomposite, (b) PXRD patterns of ALM-Au/Pd before and after the photocatalytic reaction, (c) TEM image of ALM-Au/Pd after light irradiation and (d) the CA curves of all of the photocatalysts.



Overall reaction:



Stability and reusability of the photocatalyst

The stability of the photocatalyst in a photocatalysis reaction is an important parameter. Therefore, to evaluate stability and reusability of the ALM-Au/Pd photocatalyst for one-pot imine synthesis. The reusability experiments over the ALM-Au/Pd photocatalyst were studied under visible light irradiation for 12 h. After each run, the colloidal suspension was washed with distilled water and ethanol for the next run. The results are summarised in Fig. 10a and indicate that yields of benzaldehyde, imine and aniline do not show distinct changes during the first two cycles, and then show a slight

decreasing trend over the next two cycles. This may be due to partial loss of the catalyst during isolation. To investigate the photostability of the sample, both fresh and used photocatalysts were studied by PXRD and TEM. As shown in Fig. 10b, it can be clearly seen that after the light illumination, the intensity of the used ALM-Au/Pd nanocomposite was slightly more reduced than that of the fresh catalyst; otherwise there were no structural changes observed between them. Similarly, the TEM images (Fig. 10c) of the reused ALM-Au/Pd sample show an unchanged morphology even after a 4th run. The Au/Pd alloys did not leached out from the ALM surface after visible light irradiation. Furthermore, the photoelectrochemical stability and resistance of the catalyst was investigated by a CA study. Fig. 10d displays the corresponding chronoamperometric response of time dependence anodic photocurrent of LDH, ALM, ALM-Pd, ALM-Au, and ALM-Au/Pd. When all of the photocatalysts were irradiated with light, the anodic photocurrent was found to decrease more slowly in the ALM-Au/Pd nanocomposite than in the other photocatalysts and then became relatively stable with time, even after 300 s. The current density results exhibit a very slow attenuation and indicate that photocorrosion or reduction of the photoanodes might not occur during the reaction. From the above results it can be concluded that the ALM-Au/Pd nanocomposite is a highly stable and reusable visible light-driven photocatalyst for one-pot imine synthesis through benzaldehyde and aniline.

Conclusions

Herein, we have successfully synthesised a ALM-Au/Pd catalyst and exploited its photocatalytic activity for the one-pot conversion of benzyl alcohol and nitrobenzene to imine under visible-light irradiation. Introduction of MCM-41 into the LDH with functionalisation by amine groups provides a high surface area and Brønsted basic sites for photocatalytic reactions. The amine groups help in controlling the dispersion and size of the Au/Pd alloy nanoparticles on the LM surface. The metal-ligand supports interaction serves as an active site for the photocatalytic organic transformation reaction. Thus, surface heterogeneity by loading alloyed Au/Pd nanoparticles strongly interacts with reactant molecules and can remarkably improve the reaction activity. The *in situ* formation of imines under visible light irradiation proceeds *via* a redox reaction pathway involving sequential benzyl alcohol oxidation and nitrobenzene reduction. This work details a concept for integrating a newly designed bimetal alloyed nano-heterostructure for a tandem photoconversion reaction, resulting in imine synthesis that is an eco-friendly and competent organic synthesis process as an alternative to traditional industrial synthesis procedures.

Conflicts of interest

There are no conflicts to declare.

Acknowledgements

The authors are very much thankful to the management of SOA University for their encouragement and support. The grant from SERB project (EMR/2016/000606) are greatly acknowledged. Mr. Sriram Mansingh and Mr. Kundan Kumar Das (CNSNT, ITER, SOA Deemed to be University) are deeply acknowledged for their technical support.

References

- 1 D. Patil and S. Adimurthy, *Asian J. Org. Chem.*, 2013, 2, 726–744.
- 2 X. Lang, X. Chena and J. Zhao, *Chem. Soc. Rev.*, 2014, 43, 473–486.
- 3 C. A. Newman, J. C. Antilla, P. Chen, A. V. Predeus, L. Fielding and W. D. Wulff, *J. Am. Chem. Soc.*, 2007, 129, 7216–7217.
- 4 J. S. M. Samec, A. H. Ell and J.-E. Backvall, *Chem. – Eur. J.*, 2005, 11, 2327–2334.
- 5 J.-R. Wang, Y. Fu, B.-B. Zhang, X. Cui, L. Liu and Q.-X. Guo, *Tetrahedron Lett.*, 2006, 47, 8293–8297.
- 6 H. Yuan, W.-J. Yoo, H. Miyamura and S. Kobayashi, *J. Am. Chem. Soc.*, 2012, 134, 13970–13973.
- 7 H. Hirakawa, M. Katayama, Y. Shiraishi, H. Sakamoto, K. Wang, B. Ohtani, S. Ichikawa, S. Tanaka and T. Hira, *ACS Appl. Mater. Interfaces*, 2015, 7, 3797–3806.
- 8 Y. Shiraishi, K. Fujiwara, Y. Sugano, S. Ichikawa and T. Hirai, *ACS Catal.*, 2013, 3, 312–320.
- 9 C. Gunanathan, Y. Ben-David and D. Milstein, *Science*, 2007, 317, 790–792.
- 10 A. A. Melvin, K. Illath, T. Das, T. Raja, S. Bhattacharyya and C. S. Gopinath, *Nanoscale*, 2015, 7, 13477–13488.
- 11 P. Devaraji, N. K. Sathu and C. S. Gopinath, *ACS Catal.*, 2014, 4, 2844–2853.
- 12 Q. Xiao, S. Sarina, E. Jaatinen, J. Jia, D. P. Arnold, H. Liuc and H. Zhu, *Green Chem.*, 2014, 16, 4272–4285.
- 13 T. Jiang, C. Jia, L. Zhang, S. He, Y. Sang, H. Li, Y. Li, X. Xu and H. Liu, *Nanoscale*, 2015, 7, 209–217.
- 14 Y. Zhang and S.-J. Park, *J. Catal.*, 2017, 355, 1–10.
- 15 P. Fageria, S. Uppala, R. Nazir, S. Gangopadhyay, C.-H. Chang, M. Basu and S. Pande, *Langmuir*, 2016, 32, 10054–10064.
- 16 M. Wen, K. Mori, Y. Kuwahara and H. Yamashita, *ACS Energy Lett.*, 2017, 2, 1–7.
- 17 W. Y. Hernández, J. Lauwaert, P. V. D. Voort and A. Verberckmoes, *Green Chem.*, 2017, 19, 5269–5302.
- 18 M. J. Climent, A. Corma, S. Iborra and A. Velty, *J. Catal.*, 2004, 221, 474–482.
- 19 A. Takagaki, M. Takahashi, S. Nishimura and K. Ebitani, *ACS Catal.*, 2011, 1, 1562–1565.
- 20 E. Li, Z. Xu and V. Rudolph, *Appl. Catal., B*, 2009, 88, 42–49.
- 21 L. Mohapatra and K. M. Parida, *J. Mater. Chem. A*, 2016, 4, 10744–10766.
- 22 Z. Wang, Y. Song, J. Zou, L. Li, Y. Yu and L. Wu, *Catal. Sci. Technol.*, 2018, 8, 268–275.
- 23 L. Sobhana, M. Sarakha, V. Prevot and P. Fardima, *Appl. Clay Sci.*, 2016, 134, 120–127.
- 24 Z. Gao, R. Xie, G. Fan, L. Yang and F. Li, *ACS Sustainable Chem. Eng.*, 2017, 5, 5852–5861.
- 25 M. Sahoo and K. M. Parida, *Appl. Catal., A*, 2013, 460–461, 36–45.
- 26 S. Singha, M. Sahoo and K. M. Parida, *Dalton Trans.*, 2011, 40, 7130–7132.
- 27 D. P. Sahoo, D. Rath, B. Nanda and K. M. Parida, *RSC Adv.*, 2015, 5, 83707–83724.
- 28 P. Trens, M. L. Russell, L. Spjuth, M. J. Hudson and J.-O. Liljenzin, *Ind. Eng. Chem. Res.*, 2002, 41, 5220–5225.
- 29 K. M. Parida and D. Rath, *J. Mol. Catal.*, 2009, 310, 93–100.
- 30 X. Jin, K. Taniguchi, K. Yamaguchi and N. Mizuno, *Chem. Sci.*, 2016, 7, 5371–5383.
- 31 A.-Y. Park, H. Kwon, A. J. Woo and S.-J. Kim, *Adv. Mater.*, 2005, 17, 106–109.
- 32 L. Kuai, X. Yu, S. Wang, Y. Sang and B. Geng, *Langmuir*, 2012, 28, 7168–7173.
- 33 F. Gao and D. W. Goodman, *Chem. Soc. Rev.*, 2012, 41, 8009–8020.
- 34 R. Ferrando, J. Jellinek and R. L. Johnston, *Chem. Rev.*, 2008, 108, 845–910.
- 35 Y. Wua, X. Ye, S. Zhang, S. Meng, X. Fu, X. Wang, X. Zhang and S. Chen, *J. Catal.*, 2018, 359, 151–160.
- 36 N. Baliarsingh, L. Mohapatra and K. M. Parida, *J. Mater. Chem. A*, 2013, 1, 4236–4243.
- 37 D. P. Sahoo, S. Patnaik, D. Rath, B. Nanda and K. M. Parida, *RSC Adv.*, 2016, 6, 112602–112613.
- 38 C. Li, H. Lu, Y. Lin, X. Xie, H. Wanga and L. Wang, *RSC Adv.*, 2016, 6, 97237–97240.
- 39 X. Wang, Q. Liu, Z. Xiao, X. Chen, C. Shi, S. Tao, Y. Huang and C. Liang, *RSC Adv.*, 2014, 4, 48254–48259.
- 40 Y. W. Lee, N. H. Kim, K. Y. Lee, K. Kwon, M. Kim and S. W. Han, *J. Phys. Chem. C*, 2008, 112, 6717–6722.
- 41 J. F. Sanchez-Ramirez, *Superficies Vacio*, 2001, 13, 114–116.
- 42 P. A. Bharad, K. Sivaranjani and C. S. Gopinath, *Nanoscale*, 2015, 7, 11206–11215.
- 43 K. Sivaranjani and C. S. Gopinath, *J. Mater. Chem.*, 2011, 21, 2639–2647.
- 44 D. B. Nale, D. Rath, K. M. Parida, A. Gajengia and B. M. Bhanagea, *Catal. Sci. Technol.*, 2016, 6, 4872–4881.
- 45 K. M. Parida and L. Mohapatra, *Chem. Eng. J.*, 2012, 179, 131–139.
- 46 N. Dimitratos, A. Villa, D. Wang, F. Porta, D. S. Su and L. Prati, *J. Catal.*, 2006, 244, 113–121.
- 47 D. Wang, A. Villa, F. Porta, D. S. Su and L. Prati, *Chem. Commun.*, 2006, 1956–1958.
- 48 A. C. Pradhan, B. Nanda and K. M. Parida, *Dalton Trans.*, 2011, 40, 7348–7356.
- 49 D. B. Nale, S. Ranab, K. M. Parida and B. M. Bhanagea, *Appl. Catal., A*, 2014, 469, 340–349.
- 50 K. M. Parida and L. Mohapatra, *Dalton Trans.*, 2012, 41, 1173–1178.
- 51 B. Lu and K. Kawamoto, *Catal. Sci. Technol.*, 2014, 4, 4313–4321.

- 52 K. M. Cho, K. H. Kim, K. Park, C. Kim, S. Kim, A. Al-Saggaf, I. Gereige and H.-T. Jung, *ACS Catal.*, 2017, 7, 7064–7069.
- 53 Y. Zhang, X. He, J. Ouyang and H. Yang, *Sci. Rep.*, 2013, 3, 2948.
- 54 J. Ederer, P. Janos, P. Ecorchard, J. Tolasz, V. Stengl, H. Benes, M. Perchacz and O. Pop-Georgievski, *RSC Adv.*, 2017, 7, 12464–12473.
- 55 C. Wang, B. Ma, S. Xu, D. Li, S. He, Y. Zhao, J. Han, M. Wei, D. G. Evans and X. Duan, *Nano Energy*, 2017, 32, 463–469.
- 56 M. Lan, G. Fan, L. Yang and F. Li, *Ind. Eng. Chem. Res.*, 2014, 53, 12943–12952.
- 57 Y. Nakaia, M. Azumaa, M. Muraokaa, H. Kobayashib and S. Higashimoto, *Mol. Catal.*, 2017, 443, 203–208.
- 58 Y. Shiraishi, M. Ikeda, D. Tsukamoto, S. Tanaka and T. Hirai, *Chem. Commun.*, 2011, 47, 4811–4813.
- 59 Y. Shiraishi, M. Ikeda, D. Tsukamoto, S. Tanaka and T. Hirai, *Chem. Commun.*, 2011, 47, 4811–4813.
- 60 S. Nayak, L. Mohapatra and K. M. Parida, *J. Mater. Chem. A*, 2015, 3, 18622–18635.
- 61 M. Gratzel, *Nature*, 2001, 414, 338–344.
- 62 L. Ye, D. Wang and S. Chen, *ACS Appl. Mater. Interfaces*, 2016, 8, 5280–5289.
- 63 N. Bhandary, A. P. Singh, S. Kumar, P. P. Ingole, G. S. Thakur, A. K. Ganguli and S. Basu, *ChemSusChem*, 2016, 9, 2816–2823.
- 64 A. Furube, L. Du, K. Hara, R. Katoh and M. Tachiya, *J. Am. Chem. Soc.*, 2007, 129, 14852–14853.
- 65 C. Ling, X. Ye, J. Zhang, J. Zhang, S. Zhang, S. Meng, X. Fu and S. Chen, *Sci. Rep.*, 2017, 7, 27.